

How do hydrodynamic instabilities affect 3D transport in geophysical vortices?



Peng Wang*, Tamay M. Özgökmen

Rosenstiel School of Marine and Atmospheric Science, University of Miami, Miami, FL 33149, USA

ARTICLE INFO

Article history:

Received 23 July 2014

Received in revised form 19 January 2015

Accepted 25 January 2015

Available online 14 February 2015

Keywords:

Three-dimensional transport

Material exchange

Non-classic energy spectrum

ABSTRACT

Three-dimensional (3D) transport within geophysical vortices (e.g. ocean eddies) is important in understanding processes at a variety of scales, ranging from plankton production to climate variability. 3D transport can be affected by hydrodynamic instabilities of geophysical vortices; however, how the instabilities affecting 3D transport is not clear. Focusing on barotropic, inertial and 3D instabilities, we investigate the joint impacts of instabilities on 3D transport by using analytical methods and direct numerical simulations. We discover for the first time that material can be exchanged through 3D pathways which link a family of vortices generated by the instabilities in a single, initially unstable vortex. We also show that instabilities can increase the magnitude of vertical velocity, mixing rate and vertical material exchange. Besides, we find that instabilities can cause the kinetic energy wavenumber spectrum to have a power-law regime different than the classic regimes of $k^{-5/3}$ and k^{-3} , and propose a new energy spectrum to interpret the non-classic regime.

© 2015 Elsevier Ltd. All rights reserved.

1. Introduction

The three-dimensional (3D) transport in geophysical vortices (e.g. ocean eddies) is crucial in understanding biological primary productions, air-sea gas exchanges, global tracer budgets, ocean general circulation, and thereby, climate variability (e.g. Benitez-Nelson et al., 2007; Chelton et al., 2007; McGillicuddy et al., 2007; Small et al., 2008; Klein and Lapeyre, 2009; Viebahn and Eden, 2010; Siegel et al., 2011; Lévy et al., 2012; Mahadevan et al., 2012). The 3D transport can be affected by hydrodynamic instabilities of geophysical vortices, such as barotropic and inertial instabilities; however, how these instabilities affecting the 3D transport is not clear.

Barotropic instability in geophysical vortices has been extensively observed in laboratory experiments (e.g. Greenspan, 1969; Kloosterziel and van Heijst, 1991; Carnevale and Kloosterziel, 1994; Flór and van, 1996), from satellite/radar images (e.g. Pingree and Le Cann, 1992; Stapleton et al., 2002; Kossin and Schubert, 2004; Montgomery et al., 2006), and by numerical simulations (e.g. Carton et al., 1989; Carton and McWilliams, 1989; Orlandi and van, 1992; Kloosterziel and Carnevale, 1999; Schubert et al., 1999; Nolan and Montgomery, 2001). Barotropic instability receives well-known necessary conditions derived in

inviscid parallel shear flows, including Rayleigh inflection-point criterion (Rayleigh, 1880), Rayleigh-Kuo inflection-point criterion (Kuo, 1949) and Fjørtoft's criterion (Fjørtoft, 1950).

Centrifugal instability was explored in an inviscid swirling flow by Rayleigh (1917) who derived a necessary condition, known as Rayleigh circulation criterion. Later when studying inviscid flows between coaxial cylinders, Synge (1933) pointed out that the Rayleigh circulation criterion is also a sufficient condition if perturbations are axisymmetric. When background rotation is considered, centrifugal instability is regarded as inertial instability. Inertial instability can form vertically-stacked overturning cells of selective scales (e.g. Dunkerton, 1982; Hua et al., 1997; Afanasyev and Peltier, 1998; Orlandi and Carnevale, 1999; Bourlès et al., 2003; Griffiths, 2003; Kloosterziel and Carnevale, 2008), homogenize absolute linear/angular momentum (e.g. Griffiths, 2003; Kloosterziel et al., 2007; Kloosterziel et al., 2007; Carnevale et al., 2013), and affect mixing of biogeochemical tracers (e.g. Richards and Banks, 2002; Richards and Edwards, 2003; d'Orgeville et al., 2004).

The Rayleigh circulation criterion is, however, invalid for non-axisymmetric perturbations, and still no general stability criterion is achieved (Drazin and Reid, 2004). Non-axisymmetric perturbations of swirling flows (or asymmetric perturbations of parallel flows) can draw energy from background flows and lead to non-axisymmetric inertial instability (or asymmetric inertial instability). Here the “non-axisymmetric” (or “asymmetric”) means that the

* Corresponding author.

E-mail address: pwang@rsmas.miami.edu (P. Wang).

swirling (or parallel) flow is not uniform in the azimuthal (or along-flow) direction; we refer to the non-axisymmetric (or asymmetric) inertial instability as 3D instability. Further, from the perspective of normal-mode analysis, this 3D instability can be viewed as the combination of barotropic and inertial instabilities. Regarding the growth rate of 3D instability, there is an unsolved argument on whether the non-axisymmetric/asymmetric perturbations can own higher growth rates than that of the axisymmetric/symmetric ones (e.g. Gallaire and Chomaz, 2003; Billant and Gallaire, 2005; Bouchut et al., 2011; Ribstein et al., 2014).

The literature contains many studies on the onset of hydrodynamic instabilities, but less studies on the long-term impacts of instabilities on 3D transport. In fact, some studies have explored 3D transport within geophysical vortices, for instance, Fountain et al. (2000), Branicki and Kirwan (2010) and Pratt et al. (2014); however, these studies ignored instabilities, which may even break the vortices. Indeed, as stated by Lipphardt et al. (2008) while studying loop current rings in the Gulf of Mexico, these rings may fall apart due to instabilities, leading to material leakage.

In addition, the dynamical systems approach has been adopted to study the transport in unsteady flows by the introduction of the concept of Lagrangian coherent structures (LCS), which are actually a set of special material curves/surfaces, acting as transport barriers (e.g. Aref, 1984; Ottino, 1989; Haller and Yuan, 2000; Haller, 2001; Mezić, 2001; Wiggins, 2005; Samelson and Wiggins, 2006; Sturman et al., 2006; Aref et al., 2014). However, most geophysical LCS studies are restricted to two-dimensional (2D) flows, the result of which may not be applied to realistic 3D geophysical vortices under certain situations.

Hence, in order to better understand the material transport within geophysical vortices in the real world, at least two key factors need to be addressed, i.e. hydrodynamic instabilities and 3D flow structures. In the absence of density stratification, geophysical vortices are subject to three common types of hydrodynamic instability, i.e. barotropic, inertial and 3D instabilities. In this study, we investigate the joint impacts of these instabilities on 3D transport in geophysical vortices by using analytical methods and direct numerical simulations.

The paper is organized as follows. In Section 2, we outline the configurations of numerical experiments. In Section 3, we analyze barotropic, inertial and 3D instabilities using normal-mode method, and reproduce the characteristics of these instabilities via numerical simulations. The impacts of instabilities on 3D transport are presented in Section 4, and are discussed in Section 5. Finally, we conclude this study in Section 6.

2. Numerical model

Numerical simulations are used to study how instabilities develop and affect 3D transport in geophysical vortices. The simulations are performed by NEK5000 which is a Navier–Stokes (N–S) solver based on the spectral element method (e.g. Patera, 1984; Maday et al., 1990; Fischer, 1997). NEK5000 has been used for investigating oceanic phenomena, including gravity currents, mixed-layer instabilities (e.g. Özgökmen et al., 2007; Özgökmen et al., 2011) and, in a more relevant study to the present one, chaotic advection in an ocean eddy (Pratt et al., 2014). NEK5000 is adopted here for several reasons. First, its geometrical flexibility allows for a cylindrical domain that is natural for vortices. Second, it uses third-order semi-implicit time stepping and has high-order accuracy through spectral expansions. Last, NEK5000 can solve the 3D N–S equations without any ad hoc parameterizations. In contrast, many ocean general circulation models are subject to the hydrostatic approximation, in which a reduced form of the vertical momentum equation is used and vertical advection of tracers is

complicated because of the vertical coordinate system incorporated in these models (Chassignet et al., 2006). Also, many ocean models contain various parameterizations, particularly near the surface of the ocean; for instance, KPP (Large et al., 1994) mixing scheme is a popular parameterization suite. Here we compromise with realism by adopting an idealized flow configuration (i.e. homogeneous density and isolation from the ambient flow), but benefit from a systematic study of this highly resolved 3D, non-hydrostatic flow.

NEK5000 is configured to solve the following dimensionless equations of motion (1):

$$\frac{\partial \mathbf{u}}{\partial t} + (\mathbf{u} \cdot \nabla) \mathbf{u} = -\nabla p - Ro^{-1} \hat{\mathbf{k}} \times \mathbf{u} + Re^{-1} \nabla^2 \mathbf{u}, \quad (1a)$$

$$\nabla \cdot \mathbf{u} = 0. \quad (1b)$$

In this system, the key parameters are Rossby number and Reynolds number. The Rossby number is $Ro = U/(fL)$, where U and L are characteristic horizontal velocity and length scales, and $f = 2\Omega$ is the Coriolis parameter with Ω being the angular velocity of the system rotating about its vertical axis. The Reynolds number is $Re = UL/v$, where v is the kinematic viscosity. $\hat{\mathbf{k}}$ is the unit vector in the vertical direction. Based on parameter sensitivity tests, we use fixed $Re = 10^4$, which is large enough to permit the emergence of hydrodynamic instabilities without posing major challenges to capturing all degrees of freedom in the flow by the model resolution. In addition to Eq. (1), a passive scalar (tracer) C is used to visualize transport pathways, which requires the solution of:

$$\frac{\partial C}{\partial t} + (\mathbf{u} \cdot \nabla) C = Pe^{-1} \nabla^2 C, \quad (2)$$

where $Pe = UL/\kappa$ is the Péclet number and κ is the diffusivity of passive scalar.

The numerical domain (Fig. 1) is a cylinder with diameter $D = 4$ and height $H = 1$, and is discretized into 640 elements with more grid points at boundaries to better resolve thin boundary layers. Solutions on each element are represented by Legendre polynomials of order $N = 15$ (total 2,621,440 grid points). The domain is full of homogeneous fluid and rotates about its central axis at an angular velocity of Ω . At time = 0, a barotropic vortex is initialized in the center of the domain. The boundary conditions are free-slip on the sidewall, no-slip on the bottom, and prescribed velocity (Dirichlet) on the top. This Dirichlet boundary condition mimics a rotating disk which sustains the flow; the prescribed velocity has the same azimuthal profile with the initial vortex. As explained by Pratt et al. (2014), when a top and/or bottom Ekman layer has developed in a vortex, a secondary circulation will be created, driving a 3D overturning transport within the vortex.

To highlight the impacts of instabilities, we conduct two series of experiment listed in Table 1; one is called the target experiment in which the initial vortex is given by Eq. (3a), while the other is the control experiment in which the initial vortex is defined by Eq. (3b), shown in Fig. 2,

$$V(r) = 2r \exp(-12r^8), \quad (3a)$$

$$V(r) = 3.3r \exp(-2r^2). \quad (3b)$$

Both initial vortices are cyclonic with a core of positive vorticity and an annulus of negative vorticity outside the core, also known as the shielded vortex. The no-slip boundary condition at the bottom will interrupt the initial vortex, introducing perturbations into flows. With proper parameters (Ro, Re), the vortex in the target experiment supports the growth of perturbations to develop instabilities, whereas the vortex in the control experiment forbids instabilities.

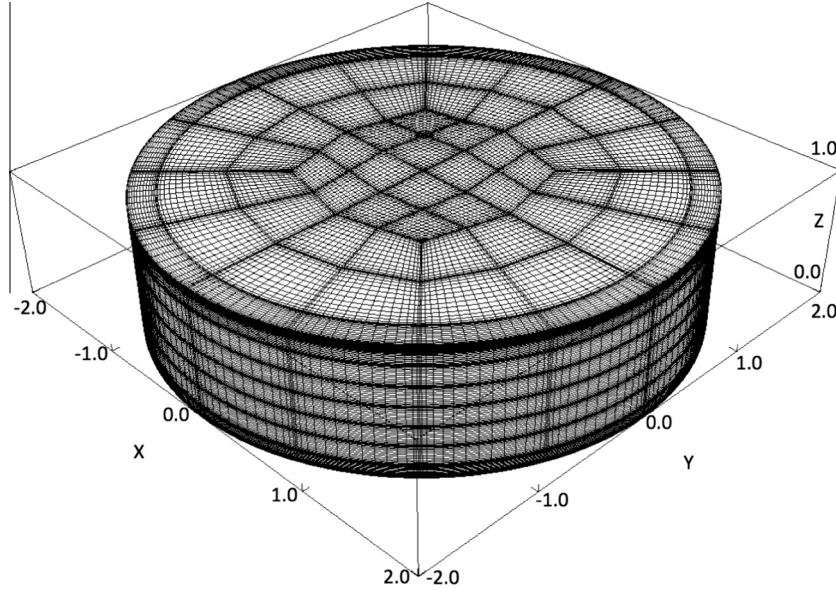


Fig. 1. The cylindrical domain of numerical experiments.

Table 1

List of the target (T) and control (C) experiments. Note that the initial vortex in the target experiment T4 is anticyclonic, denoted by “–Eq. (3a)”; that is, its flow direction is opposite to that of the flow given by Eq. (3a).

Experiment	Initial vortex profile	Ro	Re
T1	Eq. (3a)	0.2	10^4
T2	Eq. (3a)	0.04	10^4
T3	Eq. (3a)	1	10^4
T4	– Eq. (3a)	1	10^4
C1	Eq. (3b)	0.2	10^4

The numerical model is integrated with a dimensionless time step of 10^{-3} for a total integration time of 500. For the experiments listed in Table 1, the flow's kinetic energy reaches quasi-equilibrium around a integration time of 200. Furthermore, convergence checks are performed in domains of a higher resolution with polynomial order $N = 25$ (total 11,248,640 grid points) and a lower resolution with $N = 11$ (total 1,105,920 grid points). The numerical convergence is confirmed by the convergence of kinetic energy (Fig. 3).

It is worth mentioning that from the point of view of numerical configurations, the primary differences between our study and the one by Pratt et al. (2014) are the Reynolds number and initial velocity profile. In the regime of low $\text{Re} \lesssim O(10^2)$, Pratt et al. (2014) carefully investigated 3D transport inside a stable eddy. Another difference is that the initial vortex in our study is far away from domain sidewalls in order to weaken boundary effects.

3. Analysis of instabilities

Before studying the impact of instabilities on 3D transport, we present some backgrounds, such as the onset conditions, growth rates and appearance features, on these instabilities in the context of swirling flows. This helps recognize these instabilities if they appear in the numerical simulations.

3.1. Barotropic instability

Consider a circular-symmetric, inviscid vortex defined in a cylindrical coordinates (r, θ, z) . Its velocity components in the

radial (r), azimuthal (θ) and vertical/axial (z) direction are denoted by u, v, w , respectively. We analyze its barotropic instability on an f -plane using the linearized equation of quasi-geostrophic potential vorticity in shallow water systems, i.e.

$$\frac{D}{Dt} (\nabla^2 \psi' - \lambda^2 \psi') = -u' \frac{\partial}{\partial r} (\nabla^2 \bar{\psi} - \lambda^2 \bar{\psi}), \quad (4)$$

with deformation radius λ^{-1} and streamfunction $\psi(r, \theta, t) = \bar{\psi}(r) + \psi'(r, \theta, t)$, where $\bar{\psi}(r)$ is the basic-state streamfunction and $\psi'(r, \theta, t)$ represents small-amplitude perturbations. Define the perturbation of radial velocity $u' = -\frac{1}{r} \frac{\partial \psi'}{\partial \theta}$, basic-state angular velocity $\bar{\omega}(r) = \bar{v}/r$, Laplacian operator $\nabla^2 = \frac{1}{r} \left[\frac{\partial}{\partial r} \left(r \frac{\partial}{\partial r} \right) + \frac{\partial^2}{\partial \theta^2} \right]$ and $\frac{D}{Dt} = \left(\frac{\partial}{\partial t} + \frac{\bar{v}}{r} \frac{\partial}{\partial \theta} \right)$.

Seek normal-mode solution in the form of $\psi'(r, \theta, t) = \hat{\psi}(r) e^{i(m\theta - \sigma t)}$, where m is azimuthal wavenumber and $\sigma = \sigma_r + i\sigma_i$ is complex frequency. Substituting it into Eq. (4) and manipulating the equations, we obtain (cf. Appendix A)

$$\sigma_i \int \left(\frac{\frac{d}{dr} (\nabla^2 \bar{\psi} - \lambda^2 \bar{\psi})}{|\sigma - m\bar{\omega}|^2} r^2 \hat{\psi}'^2 \right) dr = 0. \quad (5)$$

Since growth rate $\sigma_i \neq 0$, the integral in Eq. (5) must be zero, yielding the necessary condition for barotropic instability; that is, the radial gradient of basic-state potential vorticity, i.e. $\frac{d}{dr} (\nabla^2 \bar{\psi} - \lambda^2 \bar{\psi})$, changes sign at least once within the domain. This condition recovers Rayleigh inflection-point criterion, if deformation radius is infinite ($\lambda = 0$).

To calculate growth rates, we choose piecewise-constant vorticity model (e.g. Michalke and Timme, 1967; Flierl, 1988; Schubert et al., 1999; Terwey and Montgomery, 2002) as the basic-state relative vorticity, i.e.

$$\bar{\zeta}(r) = \nabla^2 \bar{\psi}(r) = \begin{cases} \zeta_1 + \zeta_2 & (0 < r < r_1), \\ \zeta_2 & (r_1 < r < r_2), \\ 0 & (r_2 < r < \infty), \end{cases} \quad (6)$$

where ζ_1, ζ_2, r_1 and r_2 are constants. This vorticity model is discontinuous at inner radius r_1 and outer radius r_2 , and thus can generate edge waves to cause instability when they interact with each other

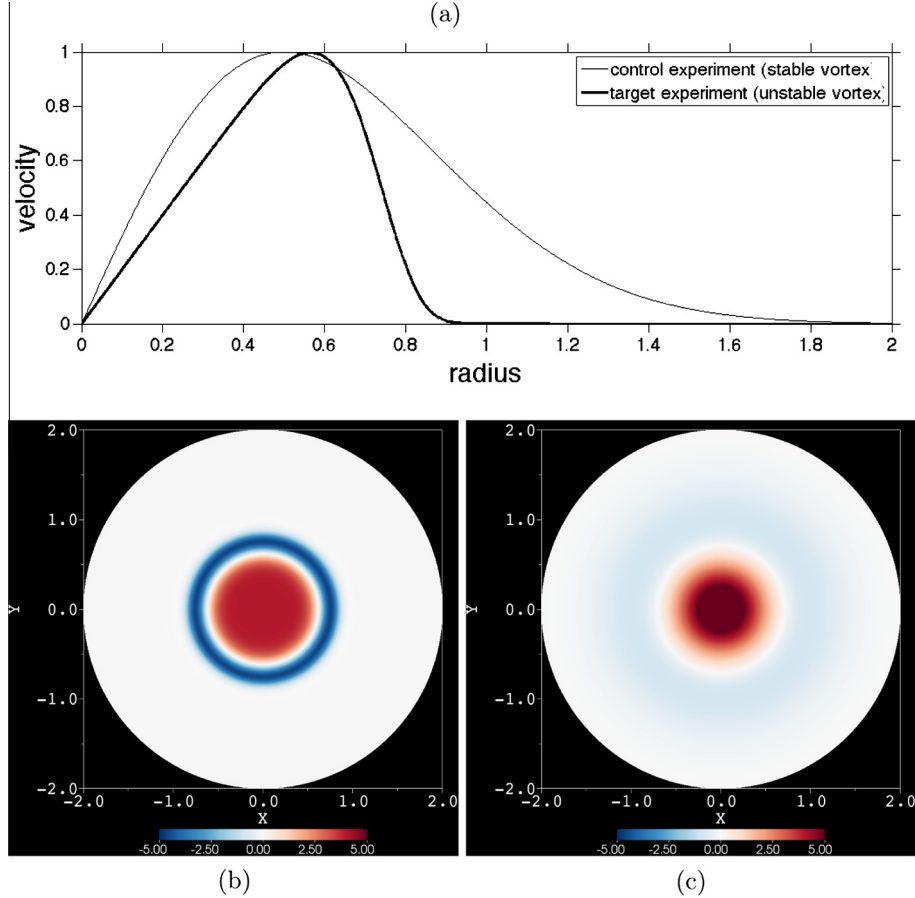


Fig. 2. (a) Initial velocity profiles of the control and target experiments. Initial vorticity fields at mid-depth horizontal plane in (b) the target experiment and (c) the control experiment.

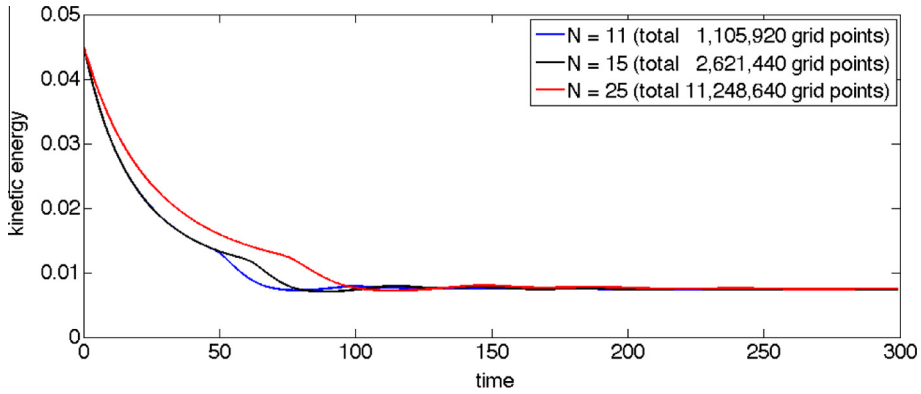


Fig. 3. An example of the numerical convergence check (from the target experiment T1). N is the order of Legendre polynomials for numerical solutions.

(Vallis, 2006). The normalized growth rate $\hat{\sigma}_i$ is defined as (cf. Appendix A),

$$\hat{\sigma}_i = \frac{\sigma_i}{|\zeta_1|} = \frac{1}{2} m \sqrt{-\left(\frac{1}{2} - G_{11} - \frac{1}{2} \delta^2 - \varepsilon G_{22}\right)^2 - 4\varepsilon G_{12}^2}, \quad (7)$$

where $\delta = r_1/r_2$ and $\varepsilon = -\zeta_2/\zeta_1$. G_{11} , G_{22} and G_{12} are given by

$$G_{ij} = I_m(\lambda r_i) K_m(\lambda r_j), \quad (i, j = 1, 2), \quad (8)$$

where $I_m(x)$ and $K_m(x)$ are modified Bessel functions of the first and second kind. As indicated by Fig. 4, the growth rate $\hat{\sigma}_i$ changes significantly with different length ratio $F = \lambda r_2$ which represents

the ratio of flow horizontal length scale to Rossby deformation radius.

Besides, an example of barotropic instability shown in Fig. 5 demonstrates that azimuthal wavenumber $m = 2$ (wavenumber-2) instability can produce two satellite vortices (of negative vorticity), while wavenumber-1 instability distorts one of the satellite vortices by shifting the central vortex towards it.

3.2. Inertial instability

Consider a vortex with a basic-state swirling flow $[0, \bar{v}(r), 0]$ which is in gradient wind balance and in hydrostatic balance. We

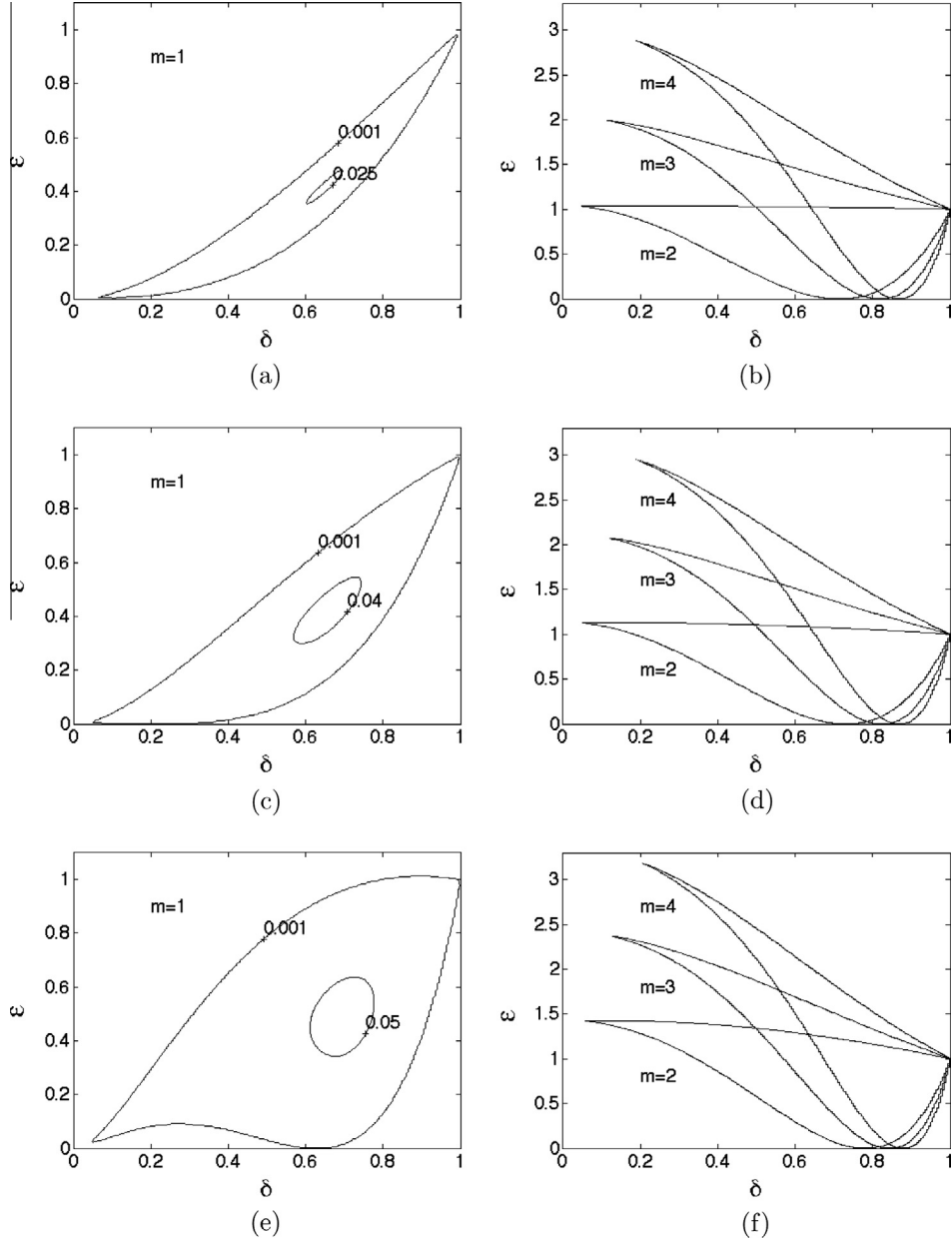


Fig. 4. Contours of normalized growth rates in $\delta - \varepsilon$ space for different azimuthal wavenumber m and length ratio F ; left column: $m = 1$, right column: $m = 2, 3, 4$; (a, b) $F = 0.5$, (c, d) $F = 1$, (e, f) $F = 2$. Closed regions have nonzero growth rate; contours in the right column depict level 0.001.

analyze its inertial instability on an f -plane in cylindrical coordinates using normal-mode method. Assume that the flow is axisymmetric ($\frac{\partial}{\partial\theta} \equiv 0$), inviscid and homogeneous, and that perturbation is $\psi'(r, z, t) = \hat{\psi}(r)e^{(\sigma_i t + ikz)}$, where σ_i is growth rate and k is vertical wavenumber. A new formula of growth rate σ_i is defined as (cf. Appendix B)

$$\sigma_i^{(n)} = \sqrt{\frac{-\Phi}{1 + \mu^{(n)}/k^2}}, \quad (n = 1, 2, 3, \dots), \quad (9)$$

where $\Phi = (2\bar{\omega} + f)(\bar{\zeta} + f)$ with basic-state angular velocity $\bar{\omega} = \bar{v}/r$, vertical vorticity $\bar{\zeta} = \frac{1}{r} \frac{d(r\bar{v})}{dr}$ and Coriolis parameter f ; $\mu^{(n)} = (x_0^{(n)}/R)^2$, where $x_0^{(n)}$ is the n th zero-crossing of Bessel function $J_1(x)$ of the first kind with order one and R is vortex radius. According to Eq. (9), for fixed vertical wavenumber k , growth rate of mode $n = 1$ is the largest, since the zero-crossings of Bessel

function increase monotonically, i.e. $x_0^{(n+1)} > x_0^{(n)} > 0$. In addition, the growth rate increases with increasing wavenumber k ; as $k \rightarrow \infty$, the growth rate σ_i reaches its upper limit $(-\Phi)^{1/2}$. Hence, the maximum growth rate that inertial instability can gain is $(-\Phi_{min})^{1/2}$, where Φ_{min} is the minimum of Φ (if $\Phi < 0$).

Inertial instability requires $\Phi < 0$ in Eq. (9), at least for one point in the domain, i.e.

$$(2\bar{\omega} + f)(\bar{\zeta} + f) < 0, \quad (10)$$

which is identical to the result obtained by Kloosterziel and van Heijst (1991) using particle-instability method. In terms of Eq. (10), we can qualitatively discuss the effect of background rotation on the inertial instability in a vortex. When $f > 0$, a cyclonic vortex has $\bar{\omega} > 0$; then background rotation (f) tries to keep both terms $(2\bar{\omega} + f)$ and $(\bar{\zeta} + f)$ to be positive, suppressing inertial instability to stabilize the cyclonic vortex. For an anticyclonic vortex ($\bar{\omega} < 0$),

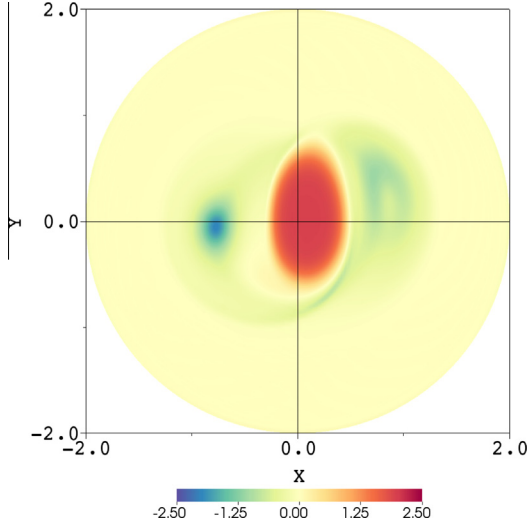


Fig. 5. Vertical vorticity at mid-depth horizontal plane from the target experiment T2, showing the asymmetric effect of azimuthal wavenumber-1 instability that shifts the central vortex off center, towards one of the two satellite vortices.

however, background rotation may stabilize or destabilize the flow depending on the micro Rossby number which is defined as $Ro_\zeta = |\zeta|/f$. If $Ro_\zeta \ll 1$, the two terms, $(2\bar{\omega} + f)$ and $(\zeta + f)$, tend to be positive, since f is dominant; therefore background rotation has stabilizing effect in this case. If $Ro_\zeta \gg 1$ then background rotation has little effect on vortex stability. If $Ro_\zeta \sim O(1)$, the above two terms are both about zero and may easily have opposite signs somewhere, causing $\Phi < 0$ and triggering inertial instability. Indeed, vigorous inertial instability in anticyclonic vortices with $Ro_\zeta \sim O(1)$ has been widely reported (e.g. Lesieur et al., 1991; Afanasyev and Peltier, 1998; Orlandi and Carnevale, 1999). In brief, background rotation has different stabilization effects on cyclonic and anticyclonic vortices, also known as selective stabilization.

Additionally, an example of inertial instability shown in Fig. 6 manifests that inertial instability can create toroidal/rib vortices that collapse later, causing vortex breaking.

3.3. Three-dimensional instability

Barotropic and inertial instabilities are essentially 2D, since flows in the analysis presented in Sections 3.1 and 3.2 are always uniform in one direction (the vertical or azimuthal). In fact, geophysical vortices may simultaneously undergo barotropic and inertial instabilities, allowing perturbations in all three directions and leading to 3D instability. Consider a vortex with a basic-state velocity $[0, \bar{v}(r), 0]$ which is in gradient wind balance and in hydrostatic balance. We analyze its stability on an f -plane in cylindrical coordinates using normal-mode method. By assuming that perturbations $\mathbf{u}'(r, \theta, z, t) = \hat{\mathbf{u}}(r)e^{i(m\theta + kz - \sigma t)}$, where m and k is azimuthal and vertical wavenumber, and $\sigma = \sigma_r + i\sigma_i$ is complex frequency, a new formula of growth rate σ_i is given by (cf. Appendix C)

$$\sigma_i = \sqrt{-\Phi \left[\frac{k^2 + (m/r)^2}{k^2 + (m/r)^2} \eta \right]}, \quad (m, k \neq 0), \quad (11)$$

where $\Phi = (2\bar{\omega} + f)(\bar{\zeta} + f)$ and $\eta = \bar{\omega}/(2\bar{\omega} + f)$ with basic-state angular velocity $\bar{\omega} = \bar{v}/r$, vertical vorticity $\bar{\zeta} = \frac{1}{r} \frac{d(r\bar{v})}{dr}$ and Coriolis parameter f . We compute the growth rate for the vortex given by Eq. (3a), with $r = 0.752$ and $\eta = 0.113$ being used in Eq. (11). This growth rate shown in Fig. 7 is similar to that of Billant and

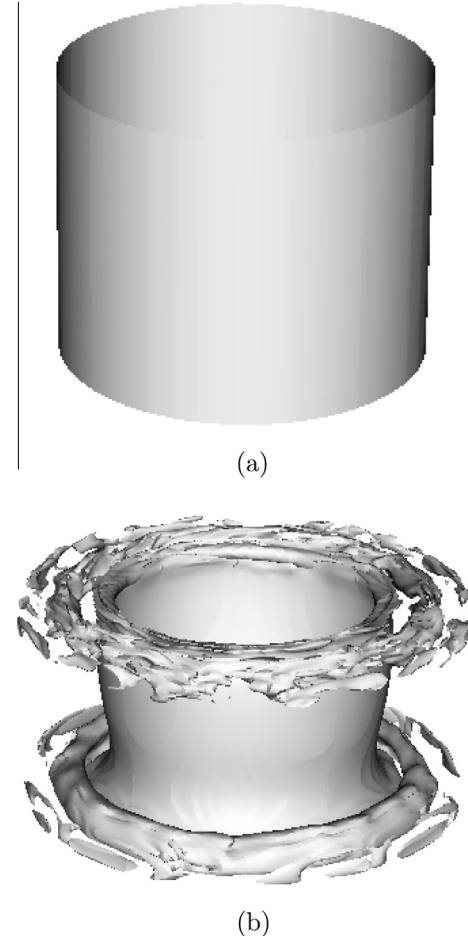


Fig. 6. The generation of toroidal/rib vortices by inertial instability from the target experiment T4, visualized by the isosurface of vertical vorticity equal to -1 at (a) time = 0 and (b) time = 8.

Gallaire (2005) who computed the growth rate using the large-axial-wavenumber WKB approximation.

In terms of Eq. (11), we can qualitatively discuss the problem on whether the non-axisymmetric/asymmetric perturbations can have higher growth rates than that of the axisymmetric/symmetric ones. In cyclonic vortices, since η satisfies the relation of $0 < \eta < 1/2$, the growth rate in Eq. (11) is less than $(-\Phi)^{1/2}$ which is the maximum growth rate for inertial instability or for axisym-

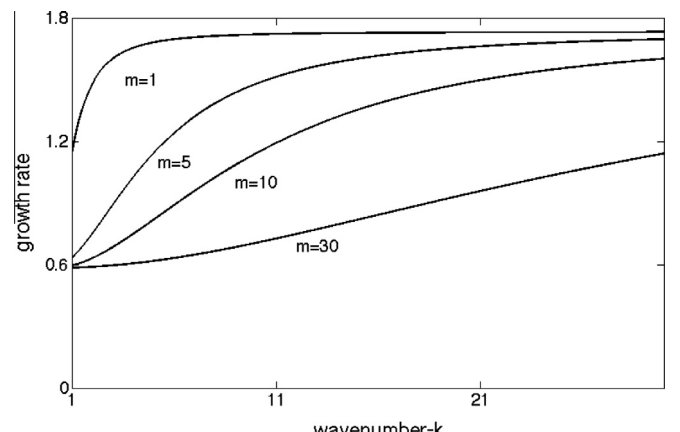


Fig. 7. Growth rates of 3D instability for different azimuthal and vertical wavenumber pairs (m, k) .

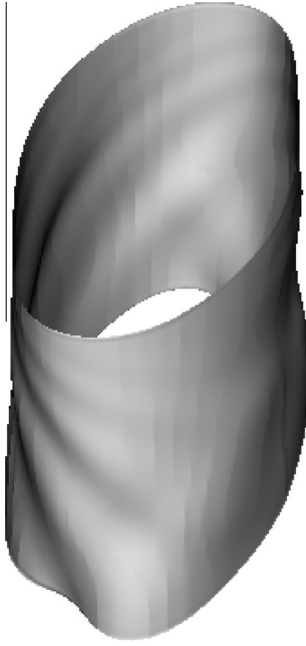


Fig. 8. The helical structure of 3D instability from the target experiment T1, visualized by the isosurface of vertical vorticity equal to 1.

metric perturbations ($m = 0$). That is to say, in cyclonic vortices, axisymmetric perturbations own the highest growth rate. Nonetheless in anticyclonic vortices, if $-\bar{\omega} < f < -2\bar{\omega}$, then $\eta > 1$; thus growth rate Eq. (11) is larger than $(-\Phi)^{-1/2}$. In other words, for anticyclonic vortices with proper η , non-axisymmetric perturbations ($m \neq 0$) can have a larger growth rate than the axisymmetric counterparts.

Further based on the growth rate in Eq. (11), we can analyze the necessary condition for the 3D instability. If taking $f > 0$, then for cyclonic vortices ($\bar{\omega} > 0$) we have $\eta > 0$; thus it requires $\Phi < 0$ at least for one point in the domain in order to get nonzero σ_i . But for anticyclonic vortices ($\bar{\omega} < 0$), $\Phi < 0$ is not necessary to launch instability because of the uncertainty of the sign of η . For example, if $\eta < 0$ and $\Phi > 0$, nonzero growth rate can still exist for proper wavenumber pairs (m, k) that satisfy $[k^2 + (m/r)^2\eta] < 0$. Hence with background rotation, anticyclonic vortices are more vulnerable to instability than the cyclonic counterparts, since anticyclonic vortices may undergo 3D instability when either $\Phi < 0$ or $\Phi > 0$.

In addition to the above necessary condition, Appendix C gives another one, which is $d\zeta/dr$ changing sign somewhere. Consequently, the 3D instability in cyclonic vortices owns two necessary conditions which are actually the necessary conditions for barotropic and inertial instabilities, respectively. This is not surprising since our stability analysis treats the 3D instability as the

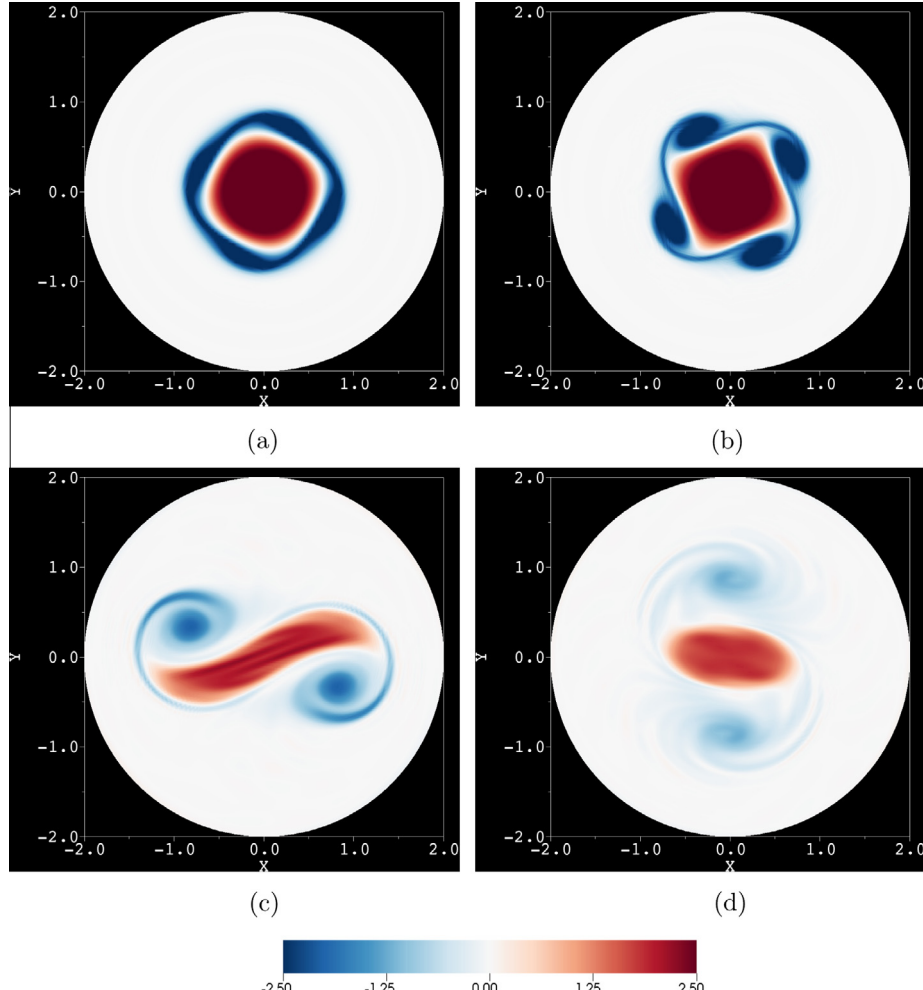


Fig. 9. Vertical vorticity field at mid-depth horizontal plane in the target experiment T1 at (a) time = 17 (b) time = 19 (c) time = 65 and (d) time = 195.

combination of barotropic and inertial instabilities. In fact, in order to combine the two kinds of instability, it requires that background flows favor both instabilities and that their growth rates are comparable.

As stated by [Gallaire and Chomaz \(2003\)](#), the 3D instability produces helical structures, each of which is associated with a specific wavenumber pair ($m \neq 0, k \neq 0$). Indeed, an example of 3D instability shown in [Fig. 8](#) exhibits such a helical structure related to the wavenumber pair ($m = 2, k = 1$).

4. Joint impacts of instabilities on transport

4.1. Evolution of an unstable vortex

In the context of the background presented in Section 3, we can now identify these instabilities developed in the vortex. Take the target experiment T1 as an example. At the beginning, the vortex undergoes weak inertial instability that generates short-living, vertically stacked overturning cells. Then barotropic instability develops the azimuthal wavenumber-4 mode ([Fig. 9a](#)) that quickly grows into nonlinear phase, creating four satellite vortices surrounding the central vortex ([Fig. 9b](#)). Through the vortex merging mechanism which states that two same-signed vorticity regions can merge into one vortex ([Melander et al., 1988](#)), the four satellite vortices merges into two larger ones. As the merging proceeds, the central vortex undergoes horizontal stretching ([Fig. 9c](#)). Next by the vortex axisymmetrization mechanism which expresses that a vortex relaxes towards axisymmetry as a result of filament generation ([Melander et al., 1987](#)), the stretched central vortex rolls up and bonds with the two satellite vortices via spiral vorticity filaments, forming tripolar vortices ([Fig. 9d](#)). The entire pattern of the tripolar vortices rotates together and remains coherent till the end of simulation. Additionally, the 3D tripolar vortices ([Fig. 10b](#)) demonstrate the helical structures produced by 3D instability. The helical structure of the central vortex has a reversed winding direction, compared with that of the satellite vortices owing to their opposite-sign vorticity.

Barotropic, inertial and 3D instabilities are all observed in the above example; accordingly, the impacts of instabilities to be presented below are actually produced by the joint actions of these instabilities.

4.2. Overturning transport by the secondary circulation

In order to visualize pathways of the overturning transport, we inject a small, low-diffusivity tracer blob within the mid-depth vortex core at the beginning, and track its evolution.

In the control experiment C1, the vertical velocity field is upward within the vortex core and downward outside the core, developing an annulus of downwelling ([Fig. 11a](#)). Thus, intuitively, tracer is transported upward within the vortex core ([Fig. 12b](#)). After arriving at the surface, tracer uniformly spreads out of the core and enters into the downwelling annulus ([Fig. 12c](#)). Then the downwelling carries tracer downward, completing the overturning transport ([Fig. 12d](#)). The above process is further illustrated via streamlines shown in [Fig. 14a](#). The streamline spirals up in the upwelling core and gets into the downwelling annulus where it spirals down.

In the target experiment T1, instabilities create small, weak downwelling zones settling in the vortex core ([Fig. 11b](#)), but the upwelling is dominant within the core. Thus, similar to the control experiment C1, the tracer goes upward at the beginning; then it is horizontally stretched ([Fig. 13b](#)) as the vortex core is suffering stretch (cf. [Fig. 9c](#)). Next due to vortex axisymmetrization, the stretched tracer rolls up, creating spiral filaments ([Fig. 13c](#)). Tails

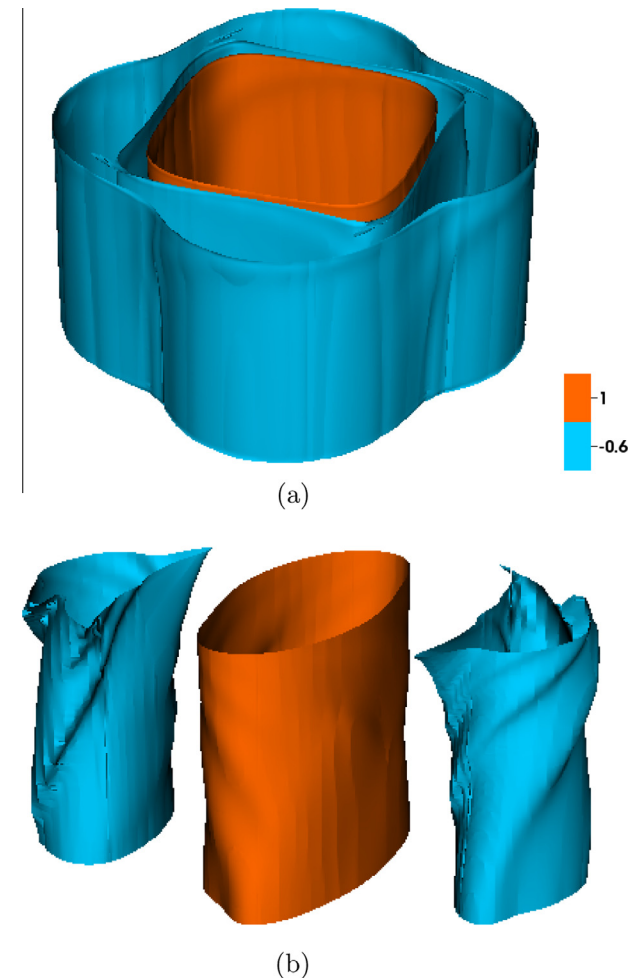


Fig. 10. 3D structures of vortices, visualized by the isosurface of vertical vorticity, correspond to the vortex shown in (a) [Fig. 9b](#) and (b) [Fig. 9d](#).

of the spiral filaments are cut off later and stay at domain corners, being nearly motionless, as shown on [Fig. 13d–f](#). After reaching the surface, the tracer disperses out of the central vortex and gets attracted into two surrounding satellite vortices ([Fig. 13d](#)), within which tracer continues moving down. During the downward motion, the tracer is gradually shaped into two 3D “funnel” structures ([Fig. 13e](#)) that are confined inside the satellite vortices. When the funnels touch the bottom, the tracer spirals inward and then is carried up by the dominant upwelling inside the central vortex ([Fig. 13f](#)). Hereafter, the tracer circulates among the central and satellite vortices and completes the overturning transport. This 3D circulation is also demonstrated by streamlines shown in [Fig. 14b](#). The two sets of streamline are parallel to each other inside the central vortex, but diverge into different satellite vortices after leaving the central vortex.

During the tracer transport, the tracer around edges of vortices quickly diffuses and mixes, implying that vigorous flow stirring (rapid stretching and folding of fluid elements) exists around edges. The finite-time Lyapunov exponent (FTLE) is adopted to test this implication. Briefly, FTLE is the exponential rate of dispersion between particles initially close to each other, after particles being advected by ambient flows for finite time (e.g. [Shadden et al., 2005](#); [Haller and Yuan, 2000](#)). The larger FTLE represents the faster particle dispersion and also means the stronger flow stirring. Indeed, as shown in [Fig. 15a](#), the extremes of FTLE occupy the regions around vortices edges, confirming the vigorous flow stirring around edges.

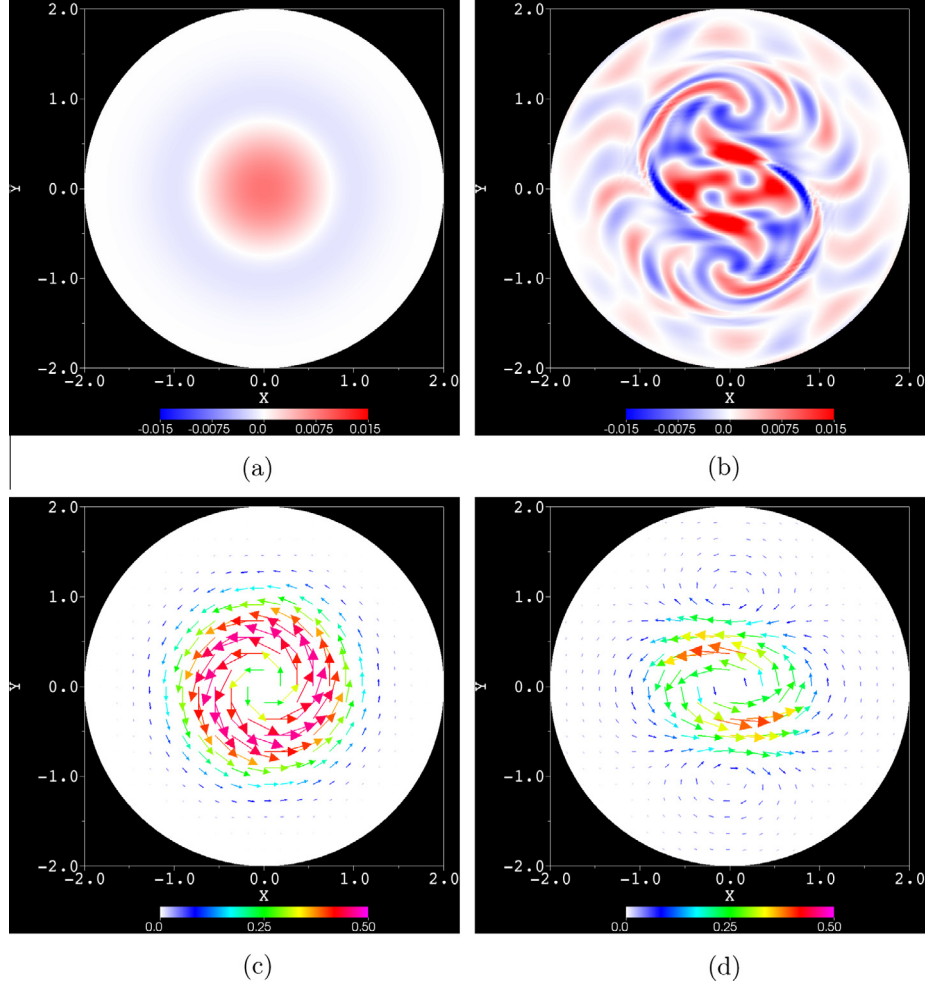


Fig. 11. (a, b) Vertical velocity fields and (c, d) horizontal velocity vectors at mid-depth horizontal plane at time = 195; color denotes the magnitude of velocity; left column: the control experiment C1; right column: the target experiment T1.

Additionally, vigorous flow stirring accompanies with strong strain rate that can be identified from Okubo–Weiss (OW) field shown in Fig. 15b. The definition of OW is $OW = S^2 - \zeta^2$, with the horizontal strain rate $S = [(u_x - v_y)^2 + (v_x + u_y)^2]^{\frac{1}{2}}$ and vertical vorticity $\zeta = v_x - u_y$ in Cartesian coordinates. Therefore, positive OW indicates strong strain rate, which appears around the edges of vortices according to Fig. 15b, particularly at the rear end of the major axis of central elliptic vortex.

Furthermore, we investigate the root mean square (RMS) of vertical velocity that reflects the flow's overall ability of vertical motions and overturning transport. In the control experiment C1, vertical velocity manifests decaying oscillations in the early adjustment stage and then gradually reaches an equilibrium (Fig. 16). Similarly in the target experiment T1, decaying oscillations appear at the beginning (cf. Fig. 16). Afterwards (time > 15), instabilities start to grow and increase the magnitude of vertical velocity; however, the magnitude decreases later ($60 < \text{time} < 110$) and then is re-elevated to a quasi-steady state at which the magnitude is twice as much as that of the control experiment C1. On the whole, instabilities increase the magnitude of vertical velocity and therefore enhance the overturning transport. The enhanced overturning transport can be verified by comparing the location of tracer blobs in the control and target experiments. Tracer blob in the target experiment T1 has already arrived at the bottom before time = 399 (cf. Fig. 13f); while in the control experiment C1, tracer blob is still on the way to bottom at time = 399 (cf. Fig. 12d).

4.3. Rates of the vertical exchange and mixing

Now we fill up the entire domain with a low-diffusivity ($Pe = 10^5$) tracer, the initial distribution of which is uniform in the horizontal direction and is linearly stratified in the vertical direction, i.e. $C(z) = 1 - z$.

By defining the rate of vertical exchange and the rate of mixing, we can quantify the instabilities impacts. The rate of vertical exchange is estimated by the vertical gradient of vertical tracer flux, i.e. $\partial(wC)/\partial z$ (of dimension $[C][T^{-1}]$) where w is vertical velocity and C denotes tracer field. In the control experiment C1, large absolute gradients are located within the vortex core and down-welling annulus (Fig. 17), which are the zones of rapid vertical exchange. In the target experiment T1, however, large absolute gradients occupy the edges of vortices, rather than the core, as well as the spiral filaments (cf. Fig. 17). This implies that instabilities create rapid vertical exchange regions concentrated along the vortex edges. Besides, according to Fig. 17, the vertical exchange rate in the target experiment T1 is one order of magnitude higher than that in the control experiment C1.

The rate of mixing is defined as $\Gamma(t) \equiv \left| \frac{1}{\Delta t} \log \left[\frac{\bar{C}(t)}{\bar{C}(t_0)} \right] \right|$, where $\bar{C}(t)$ and $\bar{C}(t_0)$ represent domain-averaged tracer field at time t and t_0 , and $\Delta t = t - t_0$. During the early period of instability growth (Fig. 18a), the mixing rate increases by $(\Gamma_{tar} - \Gamma_{con})/\Gamma_{con} = 140\%$ (with $\Gamma_{tar} = 1.4 \times 10^{-4}$ in the target experiment and

$\Gamma_{con} = 5.8 \times 10^{-5}$ in the control experiment). The increase of mixing rate is contributed by the larger tracer gradient that is confirmed by the RMS gradient of tracer field shown in Fig. 18b.

Since the mixing rate is also depend on tracer diffusivity, we inject tracers with different diffusivities, namely $Pe = 10^4$ and $Pe = 10^6$, to examine the dependence. Indeed, as shown in Fig. 19, the mixing rate changes strikingly with tracer diffusivity; for example, in the early period of instability growth, the mixing rate increase by 40% for the higher-diffusivity tracer (with $\Gamma_{con} = 5.0 \times 10^{-4}$ and $\Gamma_{tar} = 7.0 \times 10^{-4}$) and by 1100% for the lower-diffusivity tracer (with $\Gamma_{con} = 5.8 \times 10^{-6}$ and $\Gamma_{tar} = 7.0 \times 10^{-5}$).

4.4. A new thinking on the energy transfer

The kinetic energy wavenumber spectrum is used to check the energy transfer, and is computed as follows: sample the velocity field along the azimuthal direction which is the periodic direction of the cylindrical domain, calculate the energy spectrum, and then average the spectrum over different depths in the fluid interior.

For both the control and target experiments, the initial vortices are purely axisymmetric, which theoretically means the initial flow contains the only mode of azimuthal wavenumber-0; hence, energy has the only peak at wavenumber-0 and is almost zero at other

wavenumbers. The vortex in the control experiment C1 is stable and stays axisymmetric throughout the simulation, and thus it is not surprising that the final-state energy spectrum shown in Fig. 20a has almost identical shape to the initial, but with reduced energy level due to dissipation. The fact that final-state energy remains small at nonzero wavenumbers indicates that energy is

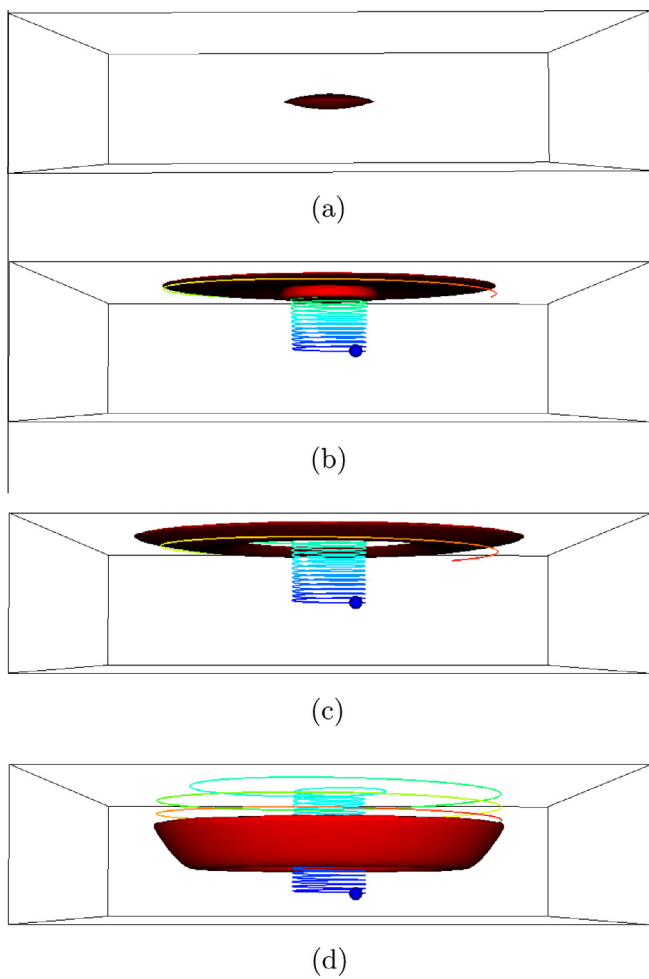


Fig. 12. Tracer evolution in the control experiment C1, visualized by the tracer isosurface of 0.0006 at (a) time = 0 (b) time = 76 (c) time = 95 and (d) time = 399. A particle trajectory is imposed on (b)–(d) with the blue sphere denoting the initial position of the particle. (Readers may refer to the animation at <http://youtu.be/qm7i0bVv41s>.)

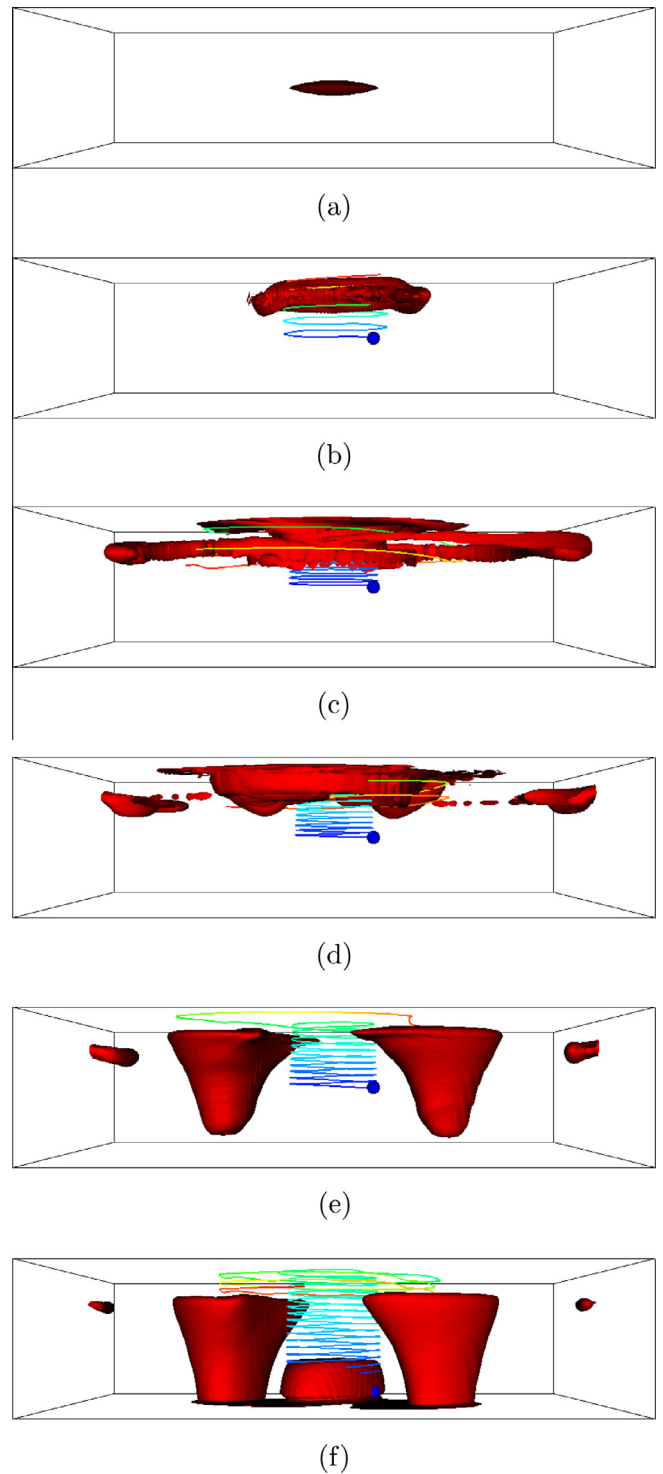


Fig. 13. Tracer evolution in the target experiment T1, visualized by the tracer isosurface of 0.0006 at (a) time = 0 (b) time = 65 (c) time = 90 (d) time = 116 (e) time = 256 and (f) time = 399. Similar to Fig. 12, a particle trajectory is imposed on (b)–(f), too. (Readers may refer to the animation at <http://youtu.be/ZJYpLcSLGSc>.)

directly dissipated by friction acting on large scales through non-local interactions (Vallis, 2006), without being cascaded into inertial ranges of energy spectrum.

On the other hand, instabilities developed in the target experiment change the flow into non-axisymmetric by generating disturbances of nonzero azimuthal wavenumbers, and increase energy at nonzero wavenumbers. Consequently, instabilities boost local nonlinear interactions, generating a broader wavenumber spectrum. We find that the final-state energy spectrum has a wavenumber power of $k^{-8/3}$ at the inertial range for the target experiment T1 (Fig. 20b) and of $k^{-7/3}$ for the target experiment T3 (Fig. 21).

We propose a heuristic explanation for the above mentioned non-classic power-law regimes of $k^{-8/3}$ and $k^{-7/3}$. Assume that through local nonlinear interactions, the quantity being transferred within the inertial range is $E^{1-\alpha}Z^\alpha$, where E is kinetic energy, Z is enstrophy and α measures the isotropy of turbulence at different wavenumbers. Postulate $\alpha \in [0, 1]$ with $\alpha = 0$ implying fully 3D isotropic turbulence and $\alpha = 1$ indicating purely 2D turbulence. Therefore, the change of α from 0 to 1 represents the transition of turbulence from 3D to 2D; that is, α bridges the gap between 3D and 2D turbulence. Denoting ξ as the transfer rate of $E^{1-\alpha}Z^\alpha$,

and using dimensional analysis, we obtain the kinetic energy spectrum

$$E(k) \propto \xi^{2/3} k^{-(4\alpha+5)/3}. \quad (12)$$

When $\alpha = 0$, the above spectrum recovers the energy-downscale-cascade regime ($k^{-5/3}$) of fully-developed, homogeneous, isotropic 3D turbulence, predicted by Kolmogorov (1941) who assumed the spectrum depends only on the energy transfer rate and wavenumber. When $\alpha = 1$, it recovers the enstrophy-downscale-cascade regime (k^{-3}) of purely 2D turbulence, predicted by Kraichnan (1967) who supposed the spectrum relies only on the enstrophy transfer rate and wavenumber. Moreover, when $\alpha = 3/4$ and $1/2$, it explains the power-law regime of $k^{-8/3}$ and $k^{-7/3}$ observed in Figs. 20b and 21, respectively. Further, analogous to the definitions of energy flux $\Pi(k)$ and enstrophy flux $Y(k)$ across wavenumber k , i.e.

$$\Pi(k) \equiv \int_k^\infty T(k') dk', \quad (13a)$$

$$Y(k) \equiv \int_k^\infty k'^2 T(k') dk', \quad (13b)$$

where $T(k')$ represents the rate of energy transfer owing to nonlinear interactions (Boffetta and Ecke, 2012), we can define the flux of $E^{1-\alpha}Z^\alpha$, denoted by $A(k)$, as

$$A(k) \equiv \int_k^\infty k'^{2\alpha} T(k') dk'. \quad (14)$$

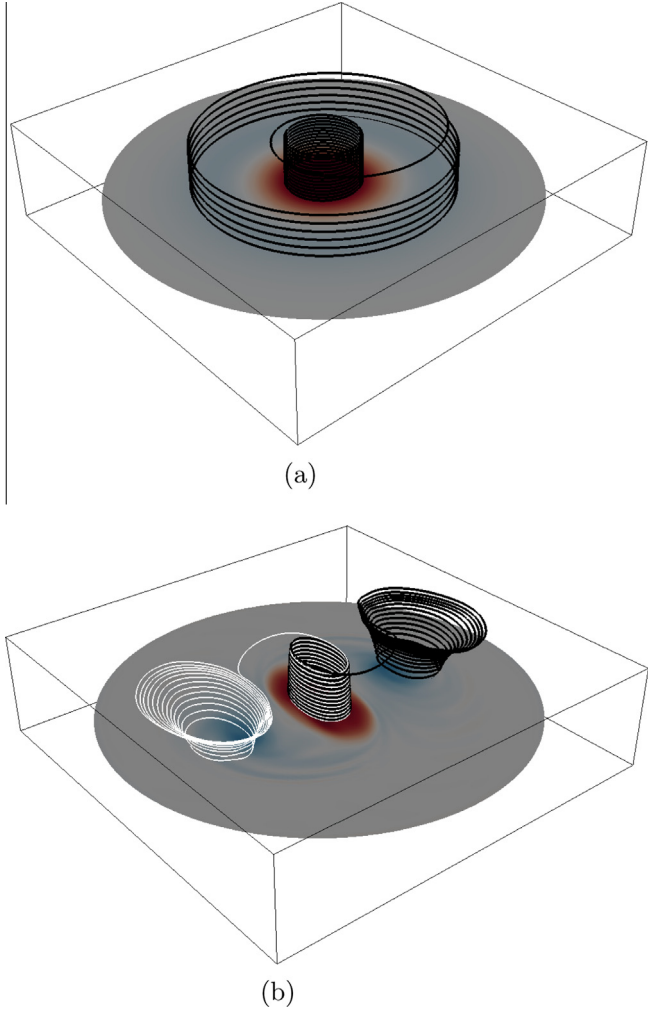


Fig. 14. Streamlines over a horizontal slice of the vertical vorticity field at mid-depth in (a) the control experiment C1 and (b) the target experiment T1 at time = 195. Two sets of streamline are coloured by red and blue. Positive (negative) vorticity is coloured by red (blue). (For interpretation of the references to colour in this figure legend, the reader is referred to the web version of this article.)

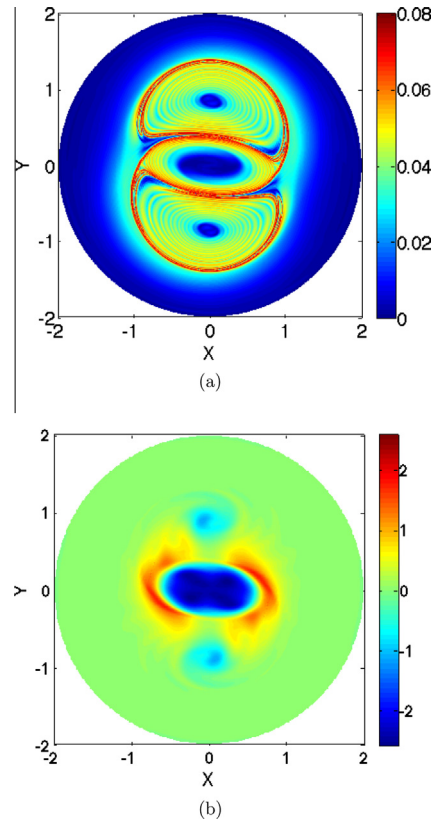


Fig. 15. (a) FTLE field at mid-depth horizontal plane in the target experiment T1 at time = 195, with trajectories of 1,283,202 particles being integrated for a period of 80 (forward-in-time). (b) Okubo-Weiss field at mid-depth horizontal plane in the target experiment T1 at time = 195.

5. Discussion

5.1. Linear instability analysis of geophysical vortices

The analysis of barotropic instability showed that wavenumber-1 instability is neutral in purely 2D flows (Schubert et al., 1999; Terwey and Montgomery, 2002). Nonetheless, laboratory experiments (Smith and Rosenbluth, 1990) and numerical simulations (Nolan and Montgomery, 2000) showed that wavenumber-1 instability has algebraic growth rate; later by numerical simulations, Nolan and Montgomery (2001) pointed out that wavenumber-1

instability may become exponentially unstable in a shallow-water system. In this study, we prove that wavenumber-1 instability can exponentially grow in shallow-water systems. Moreover, the unstable zones of wavenumber-1 instability change remarkably with Rossby radius of deformation; however, other wavenumber- m ($m = 2, 3, 4, \dots$) instabilities only alter a little (cf. Fig. 4). Therefore, wavenumber-1 instability is quite sensitive to the deformation radius, agreeing with the result of Flierl (1988).

Wavenumber-1 instability introduces geometrical asymmetry into flows by shifting the vortex core out of the symmetric center (cf. Fig. 5). This kind of asymmetry is also observed in laboratory

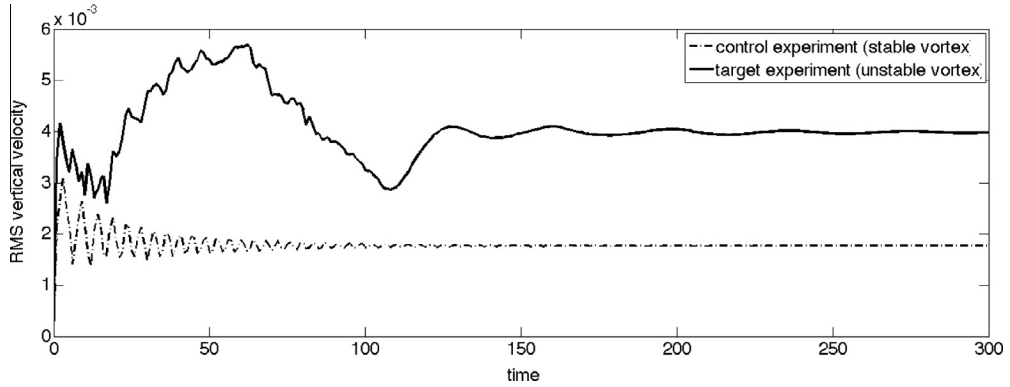


Fig. 16. Evolution of the RMS vertical velocity in the control experiment C1 and target experiment T1.

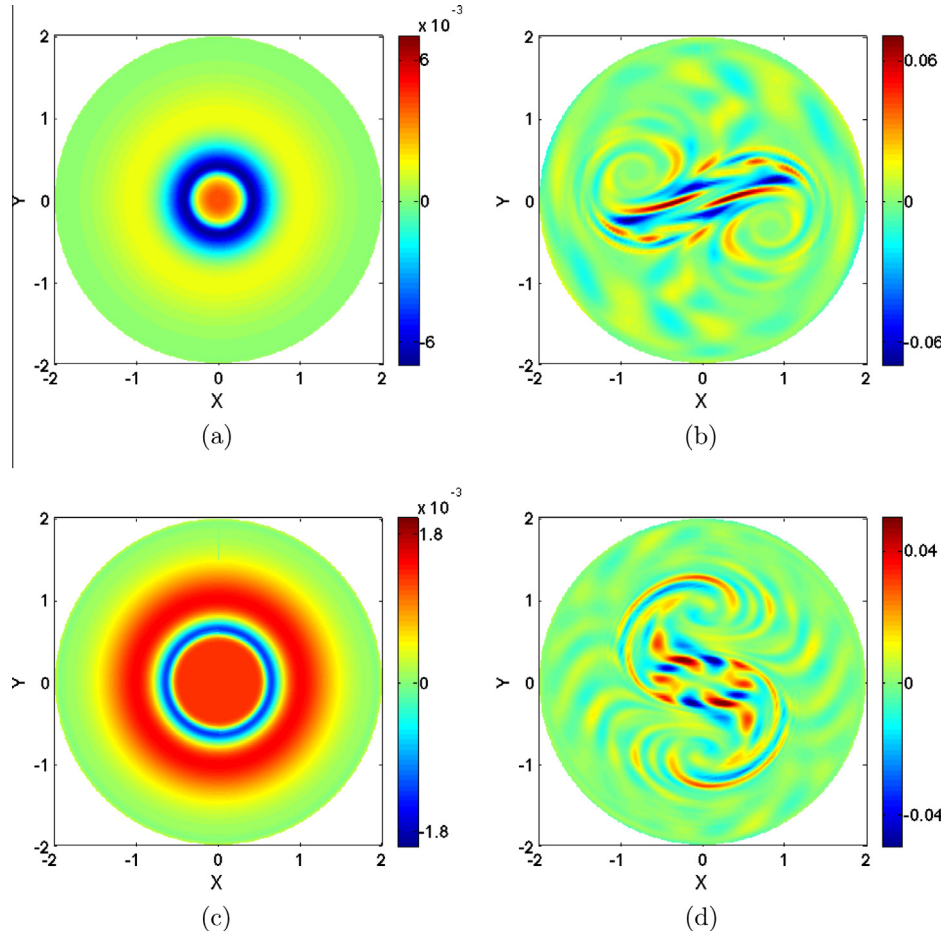


Fig. 17. Vertical gradients of the vertical tracer flux across mid-depth horizontal plane at (a, b) time = 65 and (c, d) time = 195; left column: the control experiment C1; right column: the target experiment T1.

experiment (van de Konijnengen et al., 1999, their Fig. 5) and is identified from the reflectivity map of hurricane's inner core (e.g. Reasor et al., 2000). Further, wavenumber-1 instability is claimed to be related with the trochooidal motions of hurricane tracks (Nolan and Montgomery, 2001). Analogously in ocean eddies that undergo wavenumber-1 instability, we expect that the asymmetry can be observed, for example, in ocean color images by the aid of high-resolution remote sensing technology. Also, tracks of these eddies may exhibit the wobbling motions like the hurricane tracks.

In the analysis of inertial instability (cf. Section 3.2), we discuss the selective stabilization which now is used to interpret the vorticity skewness of submesoscale turbulence. According to ship-based surveys, vorticity skewness of oceanic submesoscale turbulence is positive (towards cyclonic) in the upper ocean mixed layer and decreases to zero below the mixed layer (Shcherbina et al., 2013). Based on the selective stabilization, submesoscale anticyclonic vortices (of characteristic $Ro \sim O(1)$) are vulnerable to inertial instability under the Earth's rotation, whereas cyclonic vortices tends to be stabilized by the Earth's rotation, causing vorticity skewness towards cyclonic. Below the upper ocean mixed layer, strong density stratification prohibits inertial instability (Kloosterziel et al., 2007), and consequently anticyclonic vortices survive. Hence below the mixed layer, oceanic environments do not prefer to stabilize cyclonic or anticyclonic vortices; in other words, the vorticity skewness is about zero.

In analyzing the 3D instability which is the combination of barotropic and inertial instabilities from the perspective of normal-mode analysis, we define a new formula of growth rate. In terms of this formula, a new insight is delivered to the argument on whether the non-axisymmetric/asymmetric perturbations can

possess higher growth rates than that of the axisymmetric/symmetric ones. It was argued in swirling flows that axisymmetric perturbations own the highest growth rate at large axial/vertical wavenumbers by Gallaire and Chomaz (2003) using the direct numerical simulation of linear impulse response and by Billant and Gallaire (2005) using WKB approximation. In a jet flow study, Griffiths (2008) argued a similar conclusion which is symmetric perturbations possessing the highest growth rate at large vertical wavenumbers, by means of Rayleigh–Schrödinger perturbation analysis. In contrast, the opposite result was claimed in the study of the Bickley jet's stability; that is, asymmetric perturbations have the highest growth rate at a certain range of vertical wavenumbers (Bouchut et al., 2011; Ribstein et al., 2014). Here we suggest that the above problem should be considered separately in the context of cyclonic and anticyclonic vortices (cf. Section 3.3), at least in swirling flows. Hence, our conclusion is divided into two situations, i.e. cyclonic and anticyclonic vortices. In cyclonic vortices, axisymmetric perturbations own the highest growth rate; and in anticyclonic vortices, with the proper combination of angular velocity $\bar{\omega}$ and Coriolis parameter f that makes $\bar{\omega}/(2\bar{\omega}+f) > 1$, non-axisymmetric perturbations can have a larger growth rate.

5.2. Nonlinear evolution and transport in geophysical vortices

During the vortex evolution, we find that tracer fields tend to exhibit patterns similar to the underlying vorticity fields. For instance, temperature and pressure fields shown in Fig. 22 resemble the corresponding vorticity field shown in Fig. 9d. In fact, measuring vorticity can be quite challenging for ocean observations, while the remote sensing can readily provide estimates of the

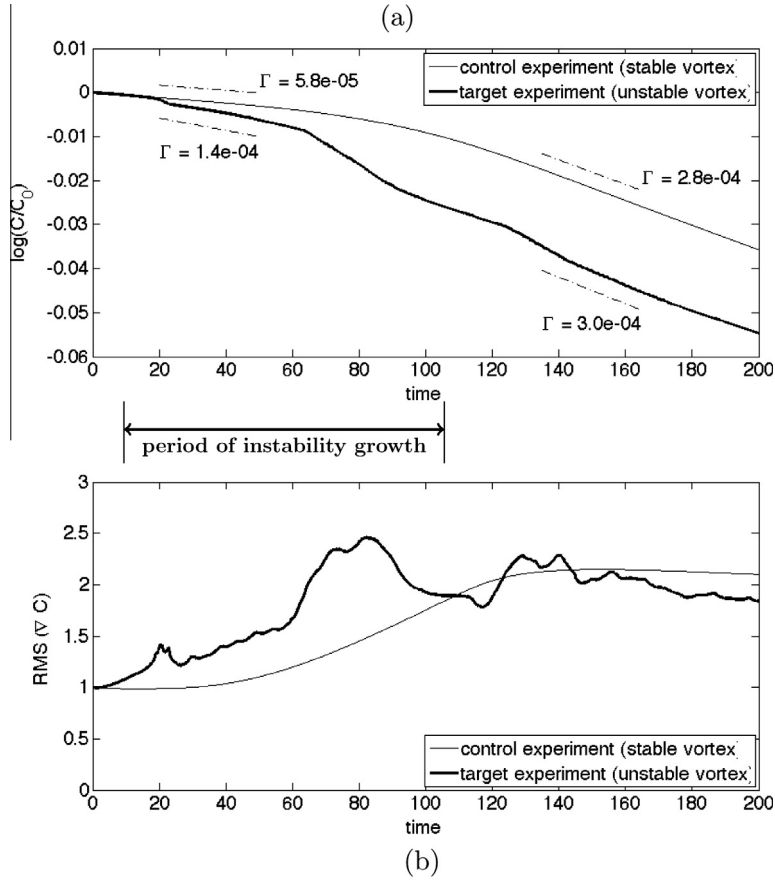


Fig. 18. (a) Evolution of the domain-averaged tracer field with mixing rate Γ being labelled; (b) evolution of the RMS gradient of tracer fields. The period of instability growth is labelled.

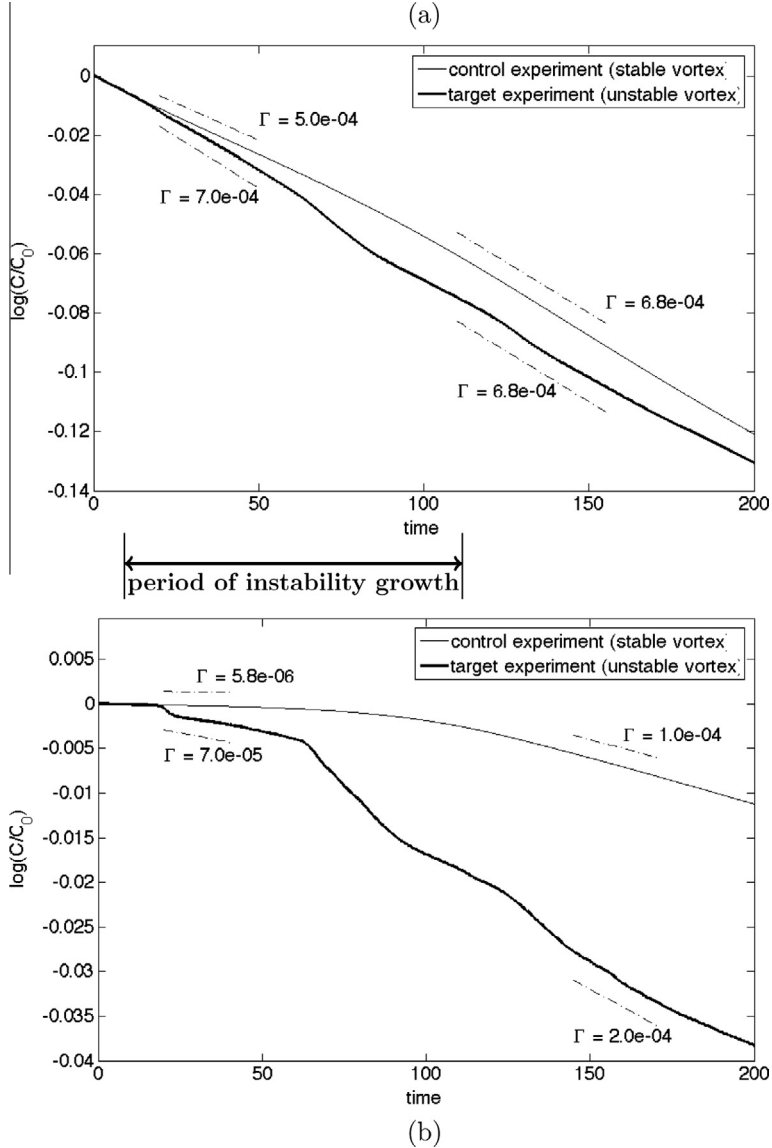


Fig. 19. Evolution of the domain-averaged tracer field with mixing rate Γ being labelled for the (a) higher diffusivity, $Pe = 10^4$ and (b) lower diffusivity, $Pe = 10^6$. The period of instability growth is labelled. (Note the different scaling of the panels.)

sea surface temperature (SST), sea surface height, chlorophyll, etc. Therefore, the pattern similarity between the vorticity field and tracer field (e.g. SST and chlorophyll) is a useful property that can help identify the united system of central and satellite vortices in the ocean. Observational examples of these united vortices were given by Pingree and Le Cann (1992, their Fig. 2) in SST and by Stapleton et al. (2002, their Fig. 2) in chlorophyll.

The tracer motion in the stable vortex (cf. Fig. 12) depicts a traditional picture of the secondary circulation within a cyclonic oceanic eddy; that is, water is uplifted in the eddy core and is pushed down at the eddy edges. If ambient surface currents exist as is in the oceanic environments, some of the uplifted water from the eddy core might be entrained into and carried away by these surface currents. Previous studies mainly focus on the upwelling branch of this secondary circulation. One reason is that the upwelling brings nutrients into euphotic zones for plankton growth, whereas the downwelling does not excite much ecosystem response (e.g. Mizobata et al., 2002; McGillicuddy et al., 2007; Klein and Lapeyre, 2009). Here our results demonstrate some interesting features of the downwelling as a result of instabilities. For example,

the downwelling shifts into the satellite eddies that are generated around the original eddy edges by instabilities. Subsequently, unexpected 3D pathways of transport, e.g. the funnels shown in Fig. 13e, are created, replacing the former downwelling annulus that is regarded as a traditional transport pathway.

Further, thinking of the material belt defined by Haller and Beron-Vera (2013) in a 2D black-hole vortex as the boundary that prevents material from leaking out of the vortex, we conclude that such material belts may also exist in the interior of 3D vortex, since material exchange between the central and satellite vortices actually take place near the 3D vortex surface and bottom, not in the interior (cf. Figs. 13e, f and 14b). Consequently, instabilities break the material belts near the 3D vortex surface and bottom, create new pathways of material exchange between the central and satellite vortices, and translate the exchange immediately into 3D regime. In this way, a family of vortices operate together in order to complete the 3D secondary circulation within this system. To our knowledge, it is the first time that this kind of cooperation among vortices has been discovered. Although previous studies found satellite vortices created by instabilities (e.g. Kloosterziel

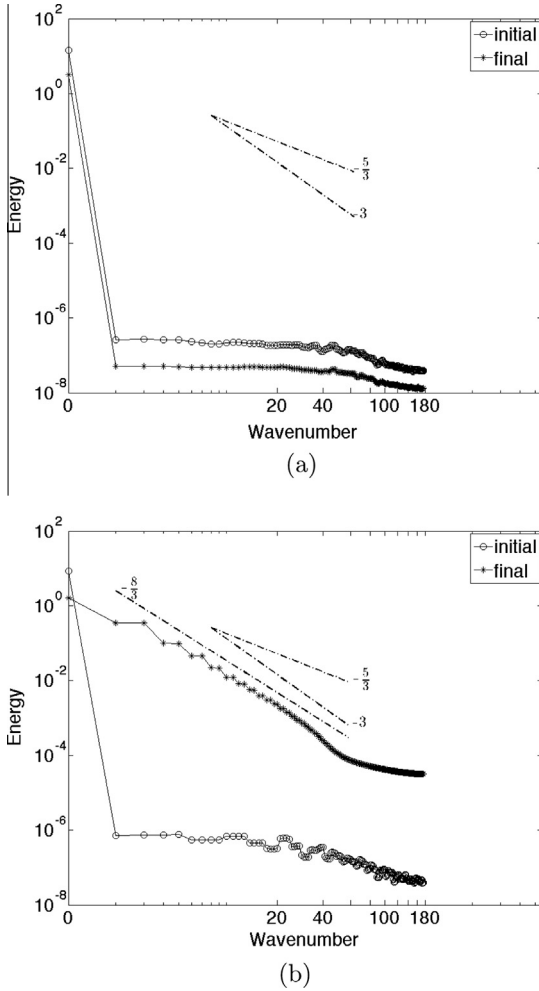


Fig. 20. Kinetic energy wavenumber spectrum at the initial and final state of the flow in (a) the control experiment C1 and (b) the target experiment T1.

and van Heijst, 1991; Carnevale and Kloosterziel, 1994; Schubert et al., 1999), the 2D kinematics and dynamics, rather than the 3D circulation, were the major concern. Besides, in order to observe a complete 3D overturning transport, the family of central and satellite vortices has to remain coherent for 10 or more eddy turnover time in our experiment. In extending the results of idealized

numerical experiments to oceanic situations, the main implication is the possibility of the existence of such complex 3D pathways for material exchange among eddies in close proximity. Indeed, such family of eddies has been captured by satellite images (e.g. Pingree and Le Cann 1992; Stapleton et al. 2002) and hopefully in the future, we can track the material exchange in these eddy families to verify this 3D pathways of transport.

The RMS vertical velocity can measure the overall ability of overturning transport by the secondary circulation. As a whole, instabilities increase the magnitude of vertical velocity; however, at a certain stage of instability growth, e.g. $60 < \text{time} < 110$ in the target experiment T1 shown in Fig. 16, the magnitude is reduced. In fact, at this stage vortex is suffering stretching (cf. Fig. 9c), which greatly depresses the upwelling in the central vortex core, causing the magnitude of vertical velocity to decrease. After the tripolar vortices have formed, the upwelling is recovered and instabilities are saturated. Hence, the magnitude of vertical velocity increases again and reaches a quasi-steady state.

Some field observations showed that strong vertical exchanges appear around the edges of mesoscale and submesoscale eddies, other than within the cores. This phenomenon has been explained by resorting to the presence of frontal instability along the periphery of eddies (e.g. Strass, 1992; Lima et al., 2002; Mizobata et al., 2002; Lapeyre and Klein, 2006; Capet et al., 2008; Klein and Lapeyre, 2009). Yet, our target experiments with homogeneous-density fluid show that without density stratification (thus no frontal instability), large rates of vertical exchange still exist around edges (cf. Figs. 17b and d). This result indicates that the instabilities can also create strong vertical exchanges around edges, in addition to the frontal instability.

As for mixing, we find that instabilities increase mixing rates, particularly for low-diffusivity tracers. This finding is reasonable since instabilities contribute to vigorous flow stirring that favors the generation of tracer filaments. The filaments amplify the gradient of tracer field (cf. Fig. 18b, during the period of instability growth). Large gradients of tracer field then accelerate the tracer mixing. Thus, throughout the above successive process, we can conclude that instabilities increase mixing rates. In addition, the filaments generation is of special importance to low-diffusivity tracers for mixing, unlike high-diffusivity tracers that can quickly mix, even without filaments generation, owing to their high molecular diffusion. Therefore, instabilities are more important for the mixing of low-diffusivity tracers than high-diffusivity tracers. In oceanic environments, heat diffusivity is two orders of magnitude higher than salinity diffusivity; therefore, we infer that instabilities increase salinity mixing more efficiently than heat mixing.

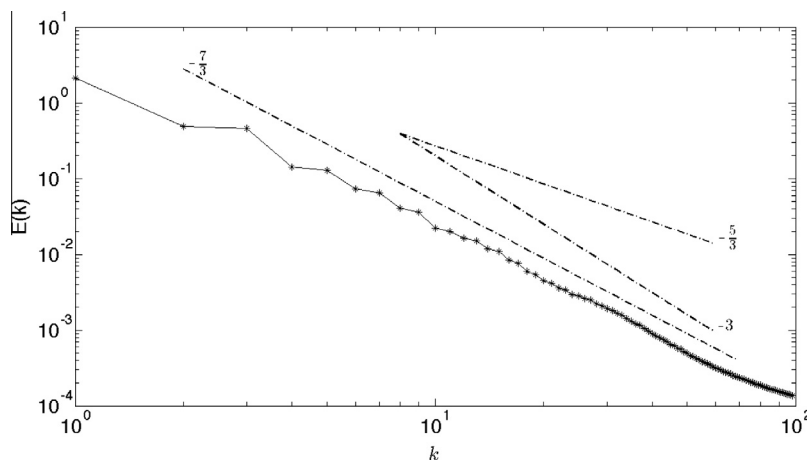


Fig. 21. Kinetic energy wavenumber spectrum at the final state of the flow in the target experiment T3.

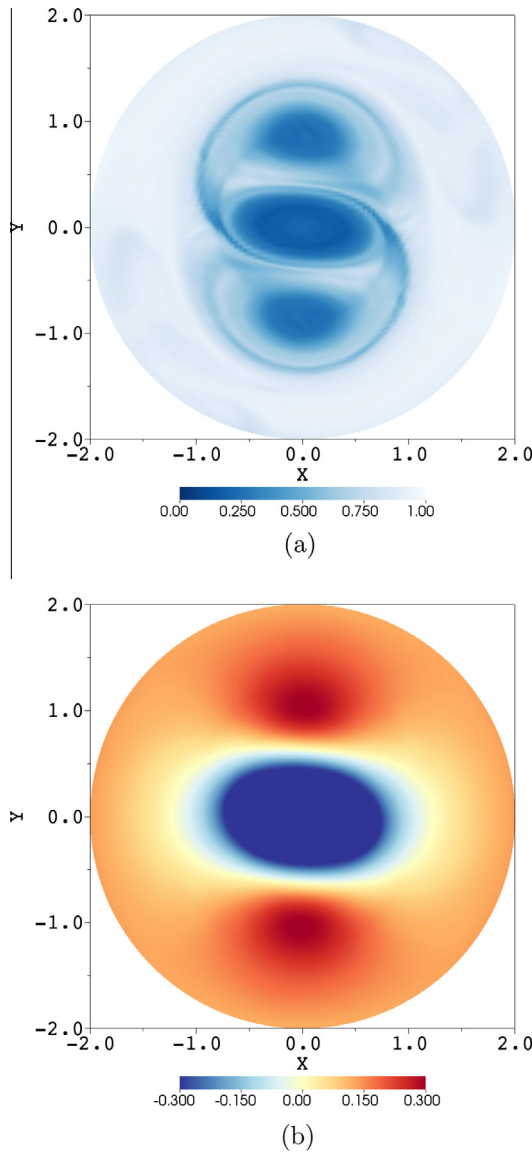


Fig. 22. (a) Temperature field and (b) pressure field at the surface in the target experiment T1 at time = 195.

We observe non-classic power-law regimes of energy spectrum (e.g. $k^{-8/3}$ and $k^{-7/3}$); in order to interpret the non-classic regimes, we propose a new spectrum of $E(k) \propto \xi^{2/3} k^{-(4\alpha+5)/3}$, by assuming the quantity of $E^{1-\alpha} Z^\alpha$ being transferred between scales (with E and Z being energy and enstrophy). In addition, another non-classic power-law regime of k^{-2} was discovered in laboratory rotating turbulence (Baroud et al., 2002) and in oceanic submesoscale turbulence (Capet et al., 2008; Shcherbina et al., 2013). In our proposed spectrum, the k^{-2} gives $\alpha = 1/4$, implying that oceanic submesoscale turbulence is neither fully 3D ($\alpha = 0$) nor purely 2D ($\alpha = 1$). Moreover, a special case is $\alpha = 1/2$ such that $E^{1/2} Z^{1/2}$ may be interpreted as helicity (velocity–vorticity-correlations); that is, helicity is transferred between scales. Indeed, it was claimed that helicity cascade can lead to the non-classic power-law regime in rotating turbulence (e.g. Brissaud et al., 1973; Bershadskii et al., 1993; Chakraborty, 2007; Mininni and Pouquet, 2009).

Furthermore, for the turbulence governed by N-S equations under stochastic power-law forcing, the renormalization group (RG) theory predicts an energy spectrum similar to our proposed

one. The RG spectrum is given by $E(k) \propto k^{1-4\epsilon/3}$, where ϵ is the power of the forcing spectrum (e.g. Fournier and Frisch, 1983; Yakhot and Orszag, 1986; Smith and Woodruff, 1998). If ϵ is replaced by $(\alpha + 2)$, then the wavenumber power in RG spectrum is identical to that in our spectrum.

The present study contains several obvious simplifications that are introduced in order to deduce clear results and make this an incremental step towards investigation of the complex structure of real-world ocean eddies. Of particular interest for further studies are two factors, the effects of density stratification and small aspect ratios, that can create a significant anisotropy (in terms of horizontal and vertical velocities and circulation time scales) in the system, as well as generating new phenomena, such as internal gravity waves and frontal instabilities. The aspect ratio used here is relevant to the eddies in the upper ocean mixed layer and shallow coastal waters; however, smaller aspect ratios that are more realistic for deep-water oceanic environments also need to be pursued. In fact, in the rotating and stratified oceanic environment, quasi-geophysical flows tend to exhibit aspect ratios of order f/N_b ($\sim 10^{-2}$, with N_b being the buoyancy frequency).

6. Conclusion

Using the normal-mode analysis, we provide new formulas of the growth rate of barotropic, inertial and 3D instabilities in geophysical vortices. Based on these formulas, some questions can be (partially) answered, such as the exponential growth of the wavenumber-1 barotropic instability, vorticity skewness of oceanic submesoscale turbulences, and growth rate of non-axisymmetric/asymmetric perturbations in 3D instability.

Through direct numerical simulations, we investigate the joint impacts of hydrodynamic instabilities on 3D transport in geophysical vortices. We discover for the first time that material circulates within a family of vortices created by instabilities of a single, initially unstable vortex. This material circulation is accomplished by 3D pathways that connect the central and satellite vortices as a united system. Our finding implies the trap of biogeochemical tracers (e.g. nutrients) inside the ocean eddies in close proximity. Additionally, we propose a new kinetic energy wavenumber spectrum to interpret the non-classic power-law regimes (such as k^{-2} , $k^{-7/3}$ and $k^{-8/3}$), by introducing a parameter that bridges the gap between fully 3D turbulence and purely 2D turbulence. In other words, our energy spectrum can represent the 3D-2D transition in rotating turbulence.

Acknowledgements

P. Wang and T. Özgökmen are grateful to the Office of Naval Research (grant #N000141110087) and the National Science Foundation (grant #DMS1025323) for supporting this study. Also, T. Özgökmen's effort has been partially funded by a grant from the BP/The Gulf of Mexico Research Initiative. We appreciate the computational time awarded by the Center for Computational Science at the University of Miami. Discussions with Drs. David Nolan and Jörg Imberger are most valued. We would like to thank two anonymous reviewers for helping improve this manuscript.

Appendix A. Barotropic instability analysis

Substituting normal-mode solution, $\psi'(r, \theta, t) = \hat{\psi}(r)e^{i(m\theta - \sigma t)}$, into Eq. (4), we obtain

$$(\sigma - m\bar{\omega}) \left[r \frac{d}{dr} \left(r \frac{d\hat{\psi}}{dr} \right) - m^2 \hat{\psi} \right] + \left(mr \frac{d\bar{\zeta}}{dr} - \lambda^2 \sigma r^2 \right) \hat{\psi} = 0, \quad (\text{A.1})$$

where $\bar{\omega}(r) = \bar{v}/r$ is angular velocity and $\bar{\zeta}(r) = \nabla^2 \bar{\psi}$ is the vertical component of relative vorticity of basic-state flow.

Multiply Eq. (A.1) by $\hat{\psi}$ and integrate over domain with the condition $\hat{\psi} = 0$ at domain boundaries. Taking imaginary part of the above integral and assuming $\sigma - m\bar{\omega} \neq 0$, we get

$$\sigma_i \int \left(\frac{d\bar{\zeta}}{dr} - \lambda^2 \bar{v} r^2 \hat{\psi}^2 \right) dr = 0, \quad (\text{A.2})$$

with

$$\frac{d\bar{\zeta}}{dr} - \lambda^2 \bar{v} = \frac{d}{dr} (\nabla^2 \bar{\psi} - \lambda^2 \bar{\psi}). \quad (\text{A.3})$$

Next we choose the piecewise-constant vorticity model given by Eq. (6) as the basic-state relative vorticity to calculate growth rates. As stated by Smyth and McWilliams (1998), each unstable mode owns at least one critical radius r_c at which phase speed is equal to the basic-state angular velocity ($\sigma_r - m\bar{\omega} = 0$), i.e. Doppler-shift frequency vanishes. Critical radius could be anywhere in the domain; thus we can simplify Eq. (A.1) to (for $r \neq r_1, r_2$)

$$\frac{d^2 \hat{\psi}}{dr^2} + \frac{1}{r} \frac{d\hat{\psi}}{dr} - (\lambda^2 + \frac{m^2}{r^2}) \hat{\psi} = 0, \quad (\text{A.4})$$

which is the modified Bessel equation of order m . Since $\hat{\psi}(r)$ is bounded as $r \rightarrow 0$ and $r \rightarrow \infty$, and is continuous at r_1 and r_2 , we write the general solution of Eq. (A.4) as

$$\hat{\psi}(r) = \psi_1 B_m^{(1)}(r) + \psi_2 B_m^{(2)}(r), \quad (\text{A.5})$$

where ψ_1 and ψ_2 are constants. $B_m^{(1)}(r)$ and $B_m^{(2)}(r)$ are defined as

$$B_m^{(1)}(r) = \begin{cases} I_m(\lambda r) K_m(\lambda r_1) & (0 \leq r \leq r_1), \\ I_m(\lambda r_1) K_m(\lambda r) & (r_1 \leq r \leq \infty), \end{cases} \quad (\text{A.6a})$$

$$B_m^{(2)}(r) = \begin{cases} I_m(\lambda r) K_m(\lambda r_2) & (0 \leq r \leq r_2), \\ I_m(\lambda r_2) K_m(\lambda r) & (r_2 \leq r \leq \infty), \end{cases} \quad (\text{A.6b})$$

where $I_m(x)$ and $K_m(x)$ are modified Bessel functions of the first and second kind.

Then substitute solution (A.5) into the jump condition which is derived by integrating Eq. (A.1) across interface r_1 and r_2 , yielding

$$\begin{pmatrix} \sigma - m\bar{\omega}_1 + m\zeta_1 G_{11} & m\zeta_1 G_{12} \\ m\zeta_2 G_{12} & \sigma - m\bar{\omega}_2 + m\zeta_2 G_{22} \end{pmatrix} \begin{pmatrix} \psi_1 \\ \psi_2 \end{pmatrix} = \begin{pmatrix} 0 \\ 0 \end{pmatrix}, \quad (\text{A.7})$$

where $\bar{\omega}_1, \bar{\omega}_2, G_{11}, G_{22}$ and G_{12} are given by

$$\bar{\omega}_i = \bar{\omega}(\lambda r_i) \quad (i = 1, 2), \quad (\text{A.8a})$$

$$G_{ij} = I_m(\lambda r_i) K_m(\lambda r_j) \quad (i, j = 1, 2). \quad (\text{A.8b})$$

The determinant of coefficient matrix of Eq. (A.7) must be zero for nontrivial ψ_1 and ψ_2 , and we obtain the dispersion relation

$$\sigma = \frac{1}{2}(\sigma_1 + \sigma_2) \pm \frac{1}{2} \sqrt{(\sigma_1 - \sigma_2)^2 + 4m^2 \zeta_1 \zeta_2 G_{12}^2}, \quad (\text{A.9})$$

where $\sigma_1 = m\bar{\omega}_1 - m\zeta_1 G_{11}$ and $\sigma_2 = m\bar{\omega}_2 - m\zeta_2 G_{22}$ are frequencies of non-interacting edge waves living at the interfaces $r = r_1, r_2$. This dispersion relation is essentially identical to that of Flierl (1988, his Eq. (3.4)) who used a different method (contour dynamics method). Instability requires that σ has nonzero imaginary part, yielding the necessary condition, i.e. $\zeta_1 \zeta_2 < 0$, for the piecewise-constant vorticity model given by Eq. (6). If deformation radius approaches infinity, we have the following equations

$$\lim_{\lambda \rightarrow 0} G_{11} = \frac{1}{2m}, \quad \lim_{\lambda \rightarrow 0} G_{22} = \frac{1}{2m}, \quad \lim_{\lambda \rightarrow 0} G_{12} = \left(\frac{r_1}{r_2} \right)^m \frac{1}{2m}. \quad (\text{A.10})$$

Substituting equations (A.10) into Eq. (A.9), we recover the dispersion relation which was derived by Schubert et al. (1999, their Eq. (2.10)) and Terwey and Montgomery (2002, their Eq. (8)) for purely 2D vortex flows. Furthermore, by defining $\delta = r_1/r_2$ and $\varepsilon = -\zeta_2/\zeta_1$, and dividing the imaginary part of σ in Eq. (A.9) by $|\zeta_1|$, we get the normalized growth rate

$$\hat{\sigma}_i = \frac{\sigma_i}{|\zeta_1|} = \frac{1}{2} m \sqrt{-\left(\frac{1}{2} - G_{11} - \frac{1}{2} \delta^2 - \varepsilon G_{22} \right)^2 - 4\varepsilon G_{12}^2}. \quad (\text{A.11})$$

Appendix B. Inertial instability analysis

The linearized governing equations are (primes denoting perturbations)

$$\frac{\partial u'}{\partial t} - \frac{2\bar{v}\nu'}{r} - f\nu' = -\frac{1}{\rho} \frac{\partial p'}{\partial r}, \quad (\text{B.1a})$$

$$\frac{\partial \nu'}{\partial t} + u \frac{\partial \bar{v}}{\partial r} + \frac{\bar{v}u'}{r} + fu' = 0, \quad (\text{B.1b})$$

$$\frac{\partial w'}{\partial t} = -\frac{1}{\rho} \frac{\partial p'}{\partial z}, \quad (\text{B.1c})$$

$$\frac{1}{r} \frac{\partial(ru')}{\partial r} + \frac{\partial w'}{\partial z} = 0. \quad (\text{B.1d})$$

Using Eqs. (B.1a)–(B.1c), we obtain the equation of perturbation vorticity in azimuthal direction ($\omega'_\theta = \frac{\partial u'}{\partial z} - \frac{\partial w'}{\partial r}$), i.e.

$$\frac{\partial^2 \omega'_\theta}{\partial t^2} + \Phi \frac{\partial u'}{\partial z} = 0, \quad (\text{B.2})$$

where $\Phi = (2\bar{\omega} + f)(\bar{\zeta} + f)$ with basic-state vertical vorticity $\bar{\zeta} = \frac{1}{r} \frac{d(r\nu)}{dr}$, angular velocity $\bar{\omega} = \bar{v}/r$ and Coriolis parameter f . Next, we introduce streamfunction ψ' and express $u' = -\frac{\partial \psi'}{\partial z}$, $w' = \frac{1}{r} \frac{\partial(r\nu')}{\partial r}$. Substituting the normal-mode solution, $\psi'(r, z, t) = \hat{\psi}(r)e^{(\sigma_i t + ikz)}$ where σ_i is growth rate and k is vertical wavenumber, we can rewrite Eq. (B.2) as

$$\frac{d^2 \hat{\psi}}{dr^2} + \frac{1}{r} \frac{d\hat{\psi}}{dr} + \left(\mu - \frac{1}{r^2} \right) \hat{\psi} = 0, \quad (\text{B.3})$$

where $\mu = k^2(-\Phi/\sigma_i^2 - 1)$ and $\sigma_i^2 \neq 0$. For simplicity, μ is assumed to be constant and then Eq. (B.3) can be treated as Bessel, Cauchy-Euler or modified Bessel differential equation for $\mu > 0, \mu = 0$ or $\mu < 0$, respectively. Physically, $\hat{\psi}(r)$ is bounded as $r \rightarrow 0$ and $r \rightarrow \infty$, which will be satisfied only when $\mu > 0$. Therefore, Eq. (B.3) becomes Bessel equation of order one and its solution is

$$\hat{\psi}(r) = C J_1(x) = C J_1(\sqrt{\mu}r),$$

where C is a constant and $J_1(x)$ is Bessel function of the first kind of order one. Denote the n th zero-crossing of $J_1(x)$ by $x_0^{(n)}$. With boundary condition $\hat{\psi}(R) = 0$, i.e. $J_1(\sqrt{\mu}R) = 0$, where R is vortex radius, we obtain the eigenvalue μ and growth rate σ_i of mode n ,

$$\mu^{(n)} = \left(\frac{x_0^{(n)}}{R} \right)^2, \quad \sigma_i^{(n)} = \sqrt{\frac{-\Phi}{1 + \mu^{(n)}/k^2}}, \quad (n = 1, 2, 3, \dots) \quad (\text{B.4})$$

Appendix C. Three-dimensional instability analysis

The linearized governing equations are (primes denoting perturbations)

$$\frac{\partial u'}{\partial t} + \frac{\bar{v}}{r} \frac{\partial u'}{\partial \theta} - \frac{2\bar{v}v'}{r} - f v' = -\frac{1}{\rho} \frac{\partial p'}{\partial r}, \quad (\text{C.1a})$$

$$\frac{\partial v'}{\partial t} + u' \frac{\partial \bar{v}}{\partial r} + \frac{\bar{v}}{r} \frac{\partial v'}{\partial \theta} + \frac{u' \bar{v}}{r} + fu' = -\frac{1}{\rho r} \frac{\partial p'}{\partial \theta}, \quad (\text{C.1b})$$

$$\frac{\partial w'}{\partial t} + \frac{\bar{v}}{r} \frac{\partial w'}{\partial \theta} = -\frac{1}{\rho} \frac{\partial p'}{\partial z}, \quad (\text{C.1c})$$

$$\frac{1}{r} \frac{\partial(ru')}{\partial r} + \frac{1}{r} \frac{\partial v'}{\partial \theta} + \frac{\partial w'}{\partial z} = 0. \quad (\text{C.1d})$$

Manipulating Eqs. (C.1a)–(C.1c) to eliminate variable p' , we get equations for the azimuthal and radial component of perturbation vorticity. Assume normal-mode solutions $(u', v', w') = [\hat{u}(r), \hat{v}(r), \hat{w}(r)]e^{i(m\theta+kz-\sigma t)}$, where m and k is wavenumber in the azimuthal and vertical direction, and $\sigma = \sigma_r + i\sigma_i$ is complex frequency. Substitute solutions into the new equations as well as Eq. (C.1d), apply the critical-radius relation, i.e. $\sigma_r - m\bar{\omega} = 0$, mentioned in Appendix A, and take the imaginary parts, yielding

$$\sigma_i k \hat{u} - \left(\frac{2\bar{v}}{r} + f \right) k \hat{v} + \frac{\bar{v}}{r} \frac{m}{r} \hat{w} = 0, \quad (\text{C.2a})$$

$$(\bar{\zeta} + f)k \hat{u} + \sigma_i k \hat{v} - \sigma_i \frac{m}{r} \hat{w} = 0, \quad (\text{C.2b})$$

$$\frac{m}{r} \hat{v} + k \hat{w} = 0. \quad (\text{C.2c})$$

The determinant of Eqs. (C.2) must be zero for nontrivial solution, giving growth rate

$$\sigma_i = \sqrt{-\Phi \left[\frac{k^2 + (m/r)^2}{k^2 + (m/r)^2} \eta \right]}, \quad (m, k \neq 0), \quad (\text{C.3})$$

Then using Eqs. (C.1a) and (C.1b), we get the equation for the vertical perturbation vorticity. Substituting normal-mode solutions into the new equation as well as Eq. (C.1d), and taking the real parts, we obtain

$$\frac{d(r\bar{v})}{dr} = \frac{U_0}{\sigma_i} \frac{d\bar{\zeta}}{dr}, \quad (\text{C.4})$$

where U_0 is a nonzero constant. Integrating Eq. (C.4) over $r \in (0, R)$ with boundary condition $\bar{v}(R) = 0$, we attain

$$\frac{U_0}{\sigma_i} \int_0^R \frac{d\bar{\zeta}}{dr} dr = 0. \quad (\text{C.5})$$

Since $U_0 \neq 0$, the above integral has to be zero, yielding the necessary condition, i.e., the radial gradient of basic-state vorticity, $d\bar{\zeta}/dr$, changes sign somewhere.

References

- Afanasyev, Y.D., Peltier, W.R., 1998. Three-dimensional instability of anticyclonic swirling flow in rotating fluid: laboratory experiments and related theoretical predictions. *Phys. Fluids* 10 (12), 3194–3202.
- Aref, H., 1984. Stirring by chaotic advection. *J. Fluid Mech.* 143, 1–21.
- Aref, H., Blake, J.R., Budišić, M., Cartwright, J.H., Clercx, H.J., Feudel, U., Golestanian, R., Gouillart, E., Le Guer, Y., van Heijst, G.F., Krasnopol'skaya, T.S., MacKay, R.S., Meleshko, V.V., Metcalfe, G., Mezić, I., de Moura, A.P.S., Omari, K.E., Piro, O., Speetjens, M.F.M., Sturman, R., Thiffeault, J.-L., Tuval, I., 2014. Frontiers of chaotic advection. Available from: arXiv:1403.2953 [nlin.CD].
- Baroud, C.N., Plapp, B.B., She, Z.-S., Swinney, H.L., 2002. Anomalous self-similarity in a turbulent rapidly rotating fluid. *Phys. Rev. Lett.* 88 (11), 114501.
- Benítez-Nelson, C.R., Bidigare, R.R., Dickey, T.D., Landry, M.R., Leonard, C.L., Brown, S.L., Nencioni, F., Rii, Y.M., Maiti, K., Becker, J.W., Bibby, T.S., Black, W., Cai, W., Carlson, C.A., Chen, F., Kuwahara, V.S., Mahaffey, C., McAndrew, P., Quay, P.D., Rappé, M.S., Selph, K.E., Simmons, M.P., Yang, E.J., 2007. Mesoscale eddies drive increased silica export in the subtropical Pacific Ocean. *Science* 316, 1017–1021.
- Bershadskii, A., Kit, E., Tsinober, A., 1993. Spontaneous breaking of reflexional symmetry in real quasi-two-dimensional turbulence: stochastic travelling waves and helical solitons in atmosphere and laboratory. *Proc. R. Soc. Lond. A* 441, 147–155.
- Billant, P., Gallaire, F., 2005. Generalized Rayleigh criterion for non-axisymmetric centrifugal instabilities. *J. Fluid Mech.* 542, 365–379.
- Boffetta, G., Ecke, R.E., 2012. Two-dimensional turbulence. *Annu. Rev. Fluid Mech.* 44, 427–451.
- Bouchut, F., Ribstein, B., Zeitlin, V., 2011. Inertial, barotropic, and baroclinic instabilities of the Bickley jet in two-layer rotating shallow water model. *Phys. Fluids* 23, 126601.
- Bourlès, B., Andrié, C., Gouriou, Y., Eldin, G., Du Penhoat, Y., Freudenthal, S., Dewitte, B., Gallois, F., Chuchla, R., Baurand, F., Aman, A., Kouadio, G., 2003. The deep currents in the eastern equatorial Atlantic ocean. *Geophys. Res. Lett.* 30 (5), 8002.
- Branicki, M., Kirwan Jr., A.D., 2010. Stirring: the Eckart paradigm revisited. *Int. J. Eng. Sci.* 48, 1027–1042.
- Brissaud, A., Frisch, U., Leorat, J., Lesieur, M., Mazure, A., 1973. Helicity cascades in fully developed isotropic turbulence. *Phys. Fluids* 16, 1366–1367.
- Capet, X., McWilliams, J.C., Molemaker, M.J., Shchepetkin, A.F., 2008. Mesoscale to submesoscale transition in the California current system. Part II: frontal processes. *J. Phys. Oceanogr.* 38, 44–64.
- Capet, X., McWilliams, J.C., Molemaker, M.J., Shchepetkin, A.F., 2008. Mesoscale to submesoscale transition in the California current system. Part III: energy balance and flux. *J. Phys. Oceanogr.* 38, 2256–2269.
- Carnevale, G.F., Kloosterziel, R.C., 1994. Emergence and evolution of triangular vortices. *J. Fluid Mech.* 259, 305–331.
- Carnevale, G.F., Kloosterziel, R.C., Orlandi, P., 2013. Inertial and barotropic instabilities of a free current in three-dimensional rotating flow. *J. Fluid Mech.* 725, 117–151.
- Carton, X.J., Flierl, G.R., Polvani, L.M., 1989. The generation of tripoles from unstable axisymmetric isolated vortex structures. *Europhys. Lett.* 9 (4), 339–344.
- Carton, X.J., McWilliams, J.C., 1989. Barotropic and baroclinic instabilities of axisymmetric vortices in a quasigeostrophic model. In: Nihoul, J.C.J., Jamart, B.M. (Eds.), *Mesoscale/Synoptic Coherent Structures in Geophysical Turbulence*. Elsevier, pp. 225–244.
- Chakraborty, S., 2007. Signatures of two-dimensionalisation of 3D turbulence in the presence of rotation. *EPL* 79 (1), 14002.
- Chassignet, E.P., Hurlburt, H.E., Smedstad, O.M., Halliwell, G.R., Hogan, P.J., Wallcraft, A.J., Bleck, R., 2006. Ocean prediction with the hybrid coordinate ocean model (HYCOM). *Ocean Weather Forecasting*, vol. 5. Springer, Netherlands, pp. 413–426.
- Chelton, D.B., Schlaik, M.G., Samelson, R.M., De Szoeke, R.A., 2007. Global observations of large oceanic eddies. *Geophys. Res. Lett.* 34, L15606.
- d'Orgeval, M., Hua, B.L., Schopp, R., Bunge, L., 2004. Extended deep equatorial layering as a possible imprint of inertial instability. *Geophys. Res. Lett.* 31, L22303.
- Drazin, P.G., Reid, W.H., 2004. *Hydrodynamic Stability*, second ed. Cambridge University Press.
- Dunkerton, T.J., 1982. On the inertial stability of the equatorial middle atmosphere. *J. Atmos. Sci.* 38, 2354–2364.
- Fischer, P.F., 1997. An overlapping Schwarz method for spectral element solution of the incompressible Navier–Stokes equations. *J. Comput. Phys.* 133, 84–101.
- Fjrtoft, R., 1950. Application of integral theorems in deriving criteria of stability for laminar flows and for the baroclinic circular vortex. *Geophys. Publ.* 17 (6), 5–52.
- Flierl, G.R., 1988. On the instability of geostrophic vortices. *J. Fluid Mech.* 197, 349–388.
- Flór, J.B., van Heijst, G.J.F., 1996. Stable and unstable monopolar vortices in a stratified fluid. *J. Fluid Mech.* 311, 257–287.
- Fountain, G.O., Khakhar, D.V., Mezić, I., Ottino, J.M., 2000. Chaotic mixing in a bounded three-dimensional flow. *J. Fluid Mech.* 417, 265–301.
- Fournier, J.D., Frisch, U., 1983. Remarks on the renormalization group in statistical fluid dynamics. *Phys. Rev. A* 28 (2), 1000–1002.
- Gallaire, F., Chomaz, J.M., 2003. Three-dimensional instability of isolated vortices. *Phys. Fluids* 15, 2113–2126.
- Greenspan, H.P., 1969. *The Theory of Rotating Fluids*. Cambridge University Press.
- Griffiths, S.D., 2003. Nonlinear vertical scale selection in equatorial inertial instability. *J. Atmos. Sci.* 60, 977–990.
- Griffiths, S.D., 2003. The nonlinear evolution of zonally symmetric equatorial inertial instability. *J. Fluid Mech.* 474, 245–273.
- Griffiths, S.D., 2008. The limiting form of inertial instability in geophysical flows. *J. Fluid Mech.* 605, 115–143.
- Haller, G., 2001. Distinguished material surfaces and coherent structures in three-dimensional fluid flows. *Physica D* 149, 248–277.
- Haller, G., Beron-Vera, F.J., 2013. Coherent Lagrangian vortices: the black holes of turbulence. *J. Fluid Mech.* 731, R4.
- Haller, G., Yuan, G., 2000. Lagrangian coherent structures and mixing in two-dimensional turbulence. *Physica D* 147, 352–370.
- Hua, B.L., Moore, D.W., Le Gentil, S., 1997. Inertial nonlinear equilibration of equatorial flows. *J. Fluid Mech.* 331, 345–371.
- Klein, P., Lapeyre, G., 2009. The oceanic vertical pump induced by mesoscale and submesoscale turbulence. *Annu. Rev. Mar. Sci.* 1, 351–375.
- Kloosterziel, R.C., Carnevale, G.F., 1999. On the evolution and saturation of instabilities of two-dimensional isolated circular vortices. *J. Fluid Mech.* 388, 217–257.

- Kooosterziel, R.C., Carnevale, G.F., 2008. Vertical scale selection in inertial instability. *J. Fluid Mech.* 594, 249–269.
- Kooosterziel, R.C., Carnevale, G.F., Orlandi, P., 2007. Inertial instability in rotating and stratified fluids: barotropic vortices. *J. Fluid Mech.* 583, 379–412.
- Kooosterziel, R.C., Orlandi, P., Carnevale, G.F., 2007. Saturation of inertial instability in rotating planar shear flows. *J. Fluid Mech.* 583, 413–422.
- Kooosterziel, R.C., van Heijst, G.J.F., 1991. An experimental study of unstable barotropic vortices in a rotating fluid. *J. Fluid Mech.* 223, 1–24.
- Kolmogorov, A.N., 1941. The local structure of turbulence in incompressible viscous fluid for very large Reynolds numbers. *Dokl. Akad. Nauk SSSR* 30, 299–303.
- Kossin, J.P., Schubert, W.H., 2004. Mesovortices in Hurricane Isabel. *Bull. Am. Meteor. Soc.* 85, 151–153.
- Kraichnan, R.H., 1967. Inertial ranges in two-dimensional turbulence. *Phys. Fluid* 10 (7), 1417–1423.
- Kuo, H., 1949. Dynamic instability of two-dimensional non divergent flow in a barotropic atmosphere. *J. Meteor.* 6, 105–122.
- Lapeyre, G., Klein, P., 2006. Impact of the small-scale elongated filaments on the oceanic vertical pump. *J. Mar. Res.* 64, 835–851.
- Large, W.G., McWilliams, J.C., Doney, S.C., 1994. Oceanic vertical mixing: a review and a model with a nonlocal boundary layer parameterization. *Rev. Geophys.* 32 (4), 363–403.
- Lesieur, M., Yanase, S., Métais, O., 1991. Stabilizing and destabilizing effects of a solid-body rotation on quasi-two-dimensional shear layers. *Phys. Fluid* 3 (3), 403–407.
- Lévy, M., Ferrari, R., Franks, P.J.S., Martin, A.P., Rivière, P., 2012. Bringing physics to life at the submesoscale. *Geophys. Res. Lett.* 39, L14602.
- Lima, I.D., Olson, D.B., Doney, S.C., 2002. Biological response to frontal dynamics and mesoscale variability in oligotrophic environments: biological production and community structure. *J. Geophys. Res.* 107 (C8), 3111.
- Lipphardt Jr., B.L., Poje, A.C., Kirwan Jr., A.D., Kantha, L., Zweng, M., 2008. Death of three loop current rings. *J. Mar. Res.* 66, 25–60.
- Maday, Y., Patera, A.T., Rnquist, E.M., 1990. An operator-integration-factor splitting method for time-dependent problems: application to incompressible fluid flow. *J. Sci. Comput.* 5 (4), 263–292.
- Mahadevan, A., D'Asaro, E., Lee, C., Perry, M.J., 2012. Eddy-driven stratification initiates north atlantic spring phytoplankton blooms. *Science* 337, 54–58.
- McGillicuddy, D.J., Anderson, L.A., Bates, N.R., Bibby, T., Buesseler, K.O., Carlson, C.A., Davis, C.S., Ewart, C., Falkowski, P.G., Goldthwait, S.A., Hansell, D.A., Jenkins, W.J., Johnson, R., Kosnyrev, V.K., Ledwell, J.R., Li, Q.P., Siegel, D.A., Steinberg, D.K., 2007. Eddy/Wind interactions stimulate extraordinary mid-ocean plankton blooms. *Science* 316, 1021–1026.
- Melander, M.V., Zabusky, N.J., McWilliams, J.C., 1987. Axisymmetrization and vorticity-gradient intensification of an isolated two-dimensional vortex through filamentation. *J. Fluid Mech.* 178, 137–159.
- Melander, M.V., McWilliams, J.C., Zabusky, N.J., 1988. Symmetric vortex merger in two dimensions: causes and conditions. *J. Fluid Mech.* 195, 303–340.
- Mezić, I., 2001. Chaotic advection in bounded Navier–Stokes flows. *J. Fluid Mech.* 431, 347–370.
- Michalke, A., Timme, A., 1967. On the inviscid instability of certain two-dimensional vortex-type flows. *J. Fluid Mech.* 29 (4), 647–666.
- Mininni, P.D., Pouquet, A., 2009. Helicity cascades in rotating turbulence. *Phys. Rev. E* 79, 026304.
- Mizobata, K., Saitoh, S.I., Shiomoto, A., Miyamura, T., Shiga, N., Imai, K., Toratani, M., Kajiwara, Y., Sasaoka, K., 2002. Bering Sea cyclonic and anticyclonic eddies observed during summer 2000 and 2001. *Prog. Oceanogr.* 55, 65–75.
- Montgomery, M.T., Bell, M.M., Aberson, S.D., Black, M.L., 2006. Hurricane Isabel (2003): new insights into the physics of intense storms. Part I. *Bull. Am. Meteor. Soc.* 87, 1335–1347.
- Nolan, D.S., Montgomery, M.T., 2000. The algebraic growth rate of wavenumber one disturbances in hurricane-like vortices. *J. Atmos. Sci.* 57, 3514–3538.
- Nolan, D.S., Montgomery, M.T., 2001. The wavenumber-one instability and trochoidal motion of hurricane-like vortices. *J. Atmos. Sci.* 58, 3234–3270.
- Orlandi, P., Carnevale, G.F., 1999. Evolution of isolated vortices in a rotating fluid of finite depth. *J. Fluid Mech.* 381, 239–269.
- Orlandi, P., van Heijst, G.F., 1992. Numerical simulation of tripolar vortices in 2D flow. *Fluid Dyn. Res.* 9, 179–206.
- Ottino, J.M., 1989. The Kinematics of Mixing: Stretching, Chaos and Transport. Cambridge University Press.
- Özgökmen, T.M., Iliescu, T., Fischer, P.F., Srinivasan, A., Duan, J., 2007. Large eddy simulation of stratified mixing in two-dimensional dam-break problem in a rectangular enclosed domain. *Ocean Modell.* 16, 106–140.
- Özgökmen, T.M., Poje, A.C., Fischer, P.F., Haza, A.C., 2011. Large eddy simulations of mixed layer instabilities and sampling strategies. *Ocean Modell.* 39, 311–331.
- Patera, A.T., 1984. A spectral element method for fluid dynamics: laminar flow in a channel expansion. *J. Comput. Phys.* 54, 468–488.
- Pingree, R.D., Le Cann, B., 1992. Anticyclonic eddy X91 in the southern Bay of Biscay, May 1991 to February 1992. *J. Geophys. Res.* 97, 14353–14367.
- Pratt, L.J., Rypina, I.I., Özgökmen, T.M., Wang, P., Childs, H., Bebievea, Y., 2014. Chaotic advection in a steady, three-dimensional, Ekman-driven eddy. *J. Fluid Mech.* 738, 143–183.
- Rayleigh, L., 1880. On the stability, or instability, of certain fluid motions. *Proc. London Math. Soc.* 11, 57–70.
- Rayleigh, L., 1917. On the dynamics of revolving fluids. *Proc. R. Soc. London A* 93, 148–154.
- Reasor, P.D., Montogmery, M.T., Marks Jr., F.D., Gamache, J.F., 2000. Low-wavenumber structure and evolution of the hurricane inner core observed by airborne dual-doppler radar. *Mon. Weather Rev.* 128, 1653–1680.
- Ribstein, B., Plougonven, R., Zeitlin, V., 2014. Inertial versus baroclinic instability of the Bickley jet in continuously stratified rotating fluid. *J. Fluid Mech.* 743, 1–31.
- Richards, K., Banks, H., 2002. Characteristics of interleaving in the western equatorial Pacific. *J. Geophys. Res.* 107 (C12), 3231.
- Richards, K.J., Edwards, N.R., 2003. Lateral mixing in the equatorial Pacific: the importance of inertial instability. *Geophys. Res. Lett.* 30 (17), 1888.
- Samelson, R., Wiggins, S., 2006. Lagrangian Transport in Geophysical Jets and Waves. Springer, New York.
- Schubert, W.H., Montgomery, T., Taft, R.K., Guinn, T.A., Fulton, S.R., Kossin, J.P., Edwards, J.P., 1999. Polygonal eyewalls, asymmetric eye contraction, and potential vorticity mixing in hurricanes. *J. Atmos. Sci.* 56, 1197–1223.
- Shadden, S.C., Lekien, F., Marsden, J.E., 2005. Definition and properties of Lagrangian coherent structures from finite-time Lyapunov exponents in two-dimensional aperiodic flows. *Physica D* 212, 271–304.
- Shcherbina, A.Y., D'Asaro, E.A., Lee, C.M., Klymak, J.M., Molemaker, M.J., McWilliams, J.C., 2013. Statistics of vertical velocity, divergence, and strain in a developed submesoscale turbulence field. *Geophys. Res. Lett.* 40, 4706–4711.
- Siegel, D.A., Peterson, P., McGillicuddy, D.J., Maritorena, S., Nelson, N.B., 2011. Bio-optical footprints created by mesoscale eddies in the sargasso sea. *Geophys. Res. Lett.* 38, L13608.
- Small, R.J., Deszoeke, S.P., Xie, S.P., O'Neill, L., Seo, H., Song, Q., Cornillon, P., Spall, M., Minobe, S., 2008. Air–sea interaction over ocean fronts and eddies. *Dyn. Atmos. Oceans* 45, 274–319.
- Smith, R.A., Rosenbluth, M.N., 1990. Algebraic instability of hollow electron columns and cylindrical vortices. *Phys. Rev. Lett.* 64 (6), 649–652.
- Smith, L.M., Woodruff, S.L., 1998. Renormalization-group analysis of turbulence. *Annu. Rev. Fluid Mech.* 30, 275–310.
- Smyth, W.D., McWilliams, J.C., 1998. Instability of an axisymmetric vortex in a stably stratified, rotating environment. *Theor. Comput. Fluid Dyn.* 11, 305–332.
- Stapleton, N.R., Aicken, W.T., Dovey, P.R., Scott, J.C., 2002. The use radar altimeter data in combination with other satellite sensors for routine monitoring of the ocean: case study of the northern Arabian Sea and Gulf of Oman. *Can. J. Remote Sens.* 28 (4), 567–572.
- Strass, V.H., 1992. Chlorophyll patchiness caused by mesoscale upwelling at fronts. *Deep Sea Res.* 39, 75–96.
- Sturman, R., Ottino, J.M., Wiggins, S., 2006. The Mathematical Foundations of Mixing: The Linked Twist Map as a Paradigm in Applications: Micro to Macro. Cambridge University Press, Fluids to Solids.
- Synge, J.L., 1933. The stability of heterogeneous liquids. *Trans. R. Soc. Can.* 27 (3), 1–18.
- Terwey, W.D., Montgomery, M.T., 2002. Wavenumber-2 and wavenumber-m vortex Rossby wave instabilities in a generalized three-region model. *J. Atoms. Sci.* 59, 2421–2427.
- Vallis, G.K., 2006. Atmospheric and Oceanic Fluid Dynamics. Cambridge University Press.
- van de Konijnengerg, J.A., Nielsen, A.H., Rasmussen, J.J., Stenum, B., 1999. Shear-flow instability in a rotating fluid. *J. Fluid Mech.* 387, 177–204.
- Viebahn, J., Eden, C., 2010. Towards the impact of eddies on the response of the Southern Ocean to climate change. *Ocean Modell.* 34, 150–165.
- Wiggins, S., 2005. The dynamical systems approach to Lagrangian transport in oceanic flows. *Annu. Rev. Fluid Mech.* 37, 295–328.
- Yakhot, V., Orszag, S.A., 1986. Renormalization group analysis of turbulence I. Basic theory. *J. Sci. Comput.* 1, 3–51.